UC Santa Barbara
UC Santa Barbara Previously Published Works

Title

The Role of Backbone Polarity on Aggregation and Conduction of Ions in Polymer Electrolytes

Permalink

https://escholarship.org/uc/item/841160p0

Journal

Journal of the American Chemical Society, 142(15)

ISSN

0002-7863 1520-5126

Authors

Schauser, Nicole S
Grzetic, Douglas J
Tabassum, Tarnuma
et al.

Publication Date

2020-04-03

DOI

10.1021/jacs.0c00587

Peer reviewed

The Role of Backbone Polarity on Aggregation and Conduction of Ions in Polymer Electrolytes

Nicole S. Schauser,[a,b] Douglas J. Grzetic,[b] Tarnuma Tabassum,[c] Gabrielle A. Kliegle,[b,c] My Linh Le,[a,b] Ethan M. Susca,[b] Ségolène Antoine,[b] Timothy J. Keller,[c] Kris T. Delaney,[b] Songi Han,[c] Ram Seshadri,[a,b,c] Glenn H. Fredrickson,[a,b,d] Rachel A. Segalman[a,b,d]

AUTHOR ADDRESSES [a]Materials Department, [b]Materials Research Laboratory, [c]Department of Chemistry and Biochemistry, and [d]Department of Chemical Engineering, University of California, Santa Barbara, California 93106, United States

*ghf@ucsb.edu, segalman@ucsb.edu

ABSTRACT: The usual understanding in polymer electrolyte design is that increasing the polymer dielectric constant results in reduced ion aggregation and therefore increased ionic conductivity. We demonstrate here that in a class of polymers with extensive metal-ligand coordination and tunable dielectric properties, the extent of ionic aggregation is delinked from the ionic conductivity. The polymer systems considered here comprise ether, butadiene, and siloxane backbones with grafted imidazole side-chains, with dissolved Li^+, Cu^{2+}, or Zn^{2+} salts. The nature of ion aggregation is probed using a combination of X-ray scattering, electron paramagnetic resonance (in the case where the metal cation is Cu^{2+}), and polymer field theory-based simulations. Polymers with less polar backbones (butadiene, and siloxane) show stronger ion aggregation in X-ray scattering compared to those with the more polar ether backbone. The T_g-normalized ionic conductivities were however unaffected by extent of aggregation. The results are explained on the basis of simulations which indicate that polymer backbone polarizability does impact the microstructure and the extent of ion aggregation, but does not impact percolation, leading to similar ionic conductivity regardless of the extent of ion aggregation. The results emphasize the ability to design for low polymer T_g through backbone modulation, separately from controlling ion-polymer interaction dynamics through ligand choice.

INTRODUCTION

Ion conducting polymers show great potential as electrolytes in energy storage devices because they promise increased safety, mechanical robustness and voltage stability.[1-2] Higher ionic conductivity than is currently obtainable is still a requirement for practical applications.[3] A fundamental understanding of the design principles for high-conductivity solvent-free polymer electrolytes remains elusive, although significant progress has been made both experimentally[4-8] and computationally.[6, 9-10]

Ionic conductivity in polymer electrolytes is dependent on the concentration and diffusion coefficient of the ionic species present.[11] Many factors influence these quantities, including polymer dielectric constant,[12-15] glass transition temperature, T_g,[16-18] solvation chemistry,[19-21] ion aggregation[22-23] and

molecular architecture and morphology (Figure 1).[24-27] A current challenge is to design systems that enable these factors to be separated in order to identify their respective impacts. This is difficult as many of these factors are interconnected, an example being polymer polarity and T_g.[28]
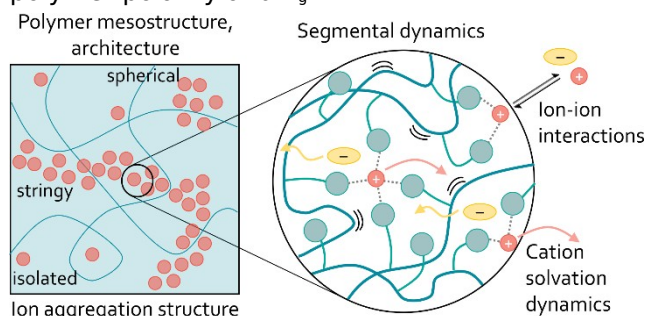

Figure 1. Polymer electrolytes often dissolve salt incompletely due to a low dielectric constant,

with ion-ion interactions resulting in aggregation. On a molecular level, the solvation site identity, polymer architecture, segmental dynamics and salt identity affect ion motion.

The extent of ion aggregation or clustering remains relatively unexplored for many reported polymer electrolytes. The lower dielectric constant of polymer electrolytes compared to organic liquid electrolytes results in incomplete salt dissociation and clustering of ionic species added to the polymer. Conflicting literature exists on whether ion clustering and aggregation negatively impacts conductivity performance. Some studies have suggested that reducing ion aggregation leads to higher ionic conductivity. For example, for a poly(ethylene oxide) (PEO)-based Li$^+$ single-ion conductor, a decrease in the polymer dielectric constant with increasing temperature led to increased ion aggregation. This clustering of ions resulted in a low mobile Li$^+$ content and low conductivity.[29-30] Ionic conductivity for this PEO-based single-ion conductor was improved upon the addition of a poly(ethylene glycol) plasticizer, due to both a lower T_g and decreased ion aggregation from charge-shielding.[31] Furthermore, molecular dynamics simulations on polyether electrolytes suggest that increasing their dielectric constant results in decreased ion aggregation and increased ionic conductivity.[32]

There are, however, other studies suggesting that aggregation can enhance ionic conductivity. Sinha and Maranas showed that for single-ion conductors based on Li$^+$, Cs$^+$ or Na$^+$, the aggregation state varied with ion identity but the ionic conductivity did not; they attributed this to an invariance of the local dynamics with ion identity as measured via quasi-elastic neutron scattering.[33] Separately, molecular dynamics simulations for single-ion anion conductors suggest that percolation of ion aggregate domains may enhance anion motion by decoupling it from polymer segmental dynamics.[34] Additionally, proton conductivity has shown to be dramatically improved in comb polymers that form aggregated nanochannels compared with similar polymers without nanoscale organization.[35] Similar trends are seen in precise ionomers forming nanoscale proton transport layers.[36] Lastly, a recent study probing the effect of linker polarity in polymeric ionic liquid networks suggested that both ion aggregation and ionic conductivity near T_g are promoted with the use of a lower polarity linker.[37]

It is very likely that ion aggregate morphology determines the impact of aggregation on ionic conductivity behavior.

Ion aggregates that form into discrete clusters, whether spherical, cylindrical or ramified, might show poor conductivity performance compared to aggregates that form percolated domains through the bulk of the electrolyte.[23, 38] This was suggested to be the cause of the improved conductivity seen in an imidazolium polymer with ions placed along the backbone rather than pendant to the backbone; changing the placement of ion groups within polymers affects the aggregation morphology, with percolated morphologies leading to improved conductivity behavior.[39-41] Aggregation morphology is challenging to measure experimentally, however, as X-ray scattering and Raman can indicate the existence but not the morphology of aggregates.[39] Some groups have obtained real-space aggregate images using electron microscopy.[42-44] However, aggregate shape is generally identified from computation rather than experiment.[39, 45]

This work analyzes the impact of aggregation on conductivity for imidazole-containing polymers with a range of polymer backbone chemistries and both mono- and multivalent salts. We have employed a versatile synthetic platform using thiol-ene click chemistry to post-functionalize polymers containing pendant vinyl groups. This enables us to study the effect of segmental dynamics and dielectric constant on ion aggregation and conductivity without changing the solvating species. We find that the backbone identity controls the dielectric constant and thus the extent of ion aggregation as probed via X-ray scattering and field-theoretic simulations.

Importantly, ion aggregation and salt identity do not correlate with ionic conductivity performance, and instead only the glass transition temperature plays a major role in determining conductivity. This study shows how polymer electrolyte design can be optimized by controlling segmental dynamics of the polymer matrix through polymer backbone choice, separately from the choice of the pendant solvating unit.

EXPERIMENTAL AND THEORETICAL METHODS

Synthesis of polymer backbones – Poly(allyl glycidyl ether) (PAGE) was synthesized via anionic ring-opening polymerization of the allyl glycidyl ether using benzyl alcohol deprotonated by potassium naphthalenide as an initiator as previously reported in the literature by Lee et al.[46] The reaction was performed at 45 °C under argon atmosphere for 24 h. The resulting PAGE was purified by precipitation in hexane and dried under

vacuum at 45 °C for 10 h. Poly(vinyl methyl siloxane) (PVMS) was synthesized by anionic polymerization using standard Schlenk line techniques. 40 mL of uninhibited and dry THF was further purified by distillation over n-butyl lithium and dried by the addition of 200 μL of sec-butyl lithium at 0 °C, after which the solution was allowed to warm to room temperature. The monomer, 1,3,5-trivinyl-1,3,5-trimethyl-cyclotrisiloxane (Gelest), was degassed by three freeze-pump-thaw cycles and used without additional purification. 200 μL of sec-butyl lithium was added to THF at 0 °C as initiator, followed by the addition of 3 mL of degassed monomer. The reaction was allowed to proceed for 3 h at 0 °C before termination with degassed methanol. The solution was concentrated and precipitated in methanol three times. Size exclusion chromatography (SEC) was performed on a Waters Alliance HPLC instrument using a refractive index detector and Agilent PLgel 5 μm MiniMIX-D column at 35 °C with THF as the eluent. Dispersity index (Đ) was determined against polystyrene calibration standards (Agilent Technologies). The PVMS molecular weight was estimated from SEC, while the PAGE molecular weight was determined using ^{1}H NMR end-group analysis (Figure S1). Poly(1,2-butadiene) (PBD) with >95% 1,2 addition, M_n = 9.5 kDa and Đ = 1.04 was purchased from Polymer Source, Inc. and used without further purification. ^{1}H NMR spectra were collected on a Varian 600 MHz spectrometer in CDCl$_3$ or DMSO-d6.

Synthesis of imidazole-functionalized polymers. N-(2-(1H-Imidazol-1-yl)propyl)-4-mercaptobutanamide (Im-SH) was synthesized as previously reported by Sanoja et al.[47] The vinyl-containing polymers were fully functionalized by UV (365 nm) activated thiol-ene click chemistry in methanol for PAGE or methanol/THF (20/80) for PBD and PVMS. The resulting polymers (PAGE-Im, PBD-Im and PVMS-Im) were purified either through dialysis in methanol (SnakeSkin dialysis tubing with a 3.5kDa MW cutoff, and solvent exchange every 12 h for a total of 5 to 7 times) or precipitation in acetonitrile, dried *in vacuo* at 55 °C in the presence of phosphorous pentoxide, and immediately transferred to a nitrogen glove box to mitigate moisture uptake.

Preparation of metal salt-containing polymers. Polymers were dissolved in anhydrous methanol and drop cast onto Teflon boats on a hot plate at 60 °C in a nitrogen atmosphere glove box. 0.05M stock solutions of Li$^+$ (Alfa Aesar), Cu^{2+} (Solvionic) and Zn^{2+} (Solvionic) bis(trifluoromethylsulfonyl)imide (TFSI$^-$) salts in anhydrous methanol were added to the Teflon boats in appropriate amounts to reach nominal metal cation-to-imidazole molar ratios, *r*, of 0.03, 0.08 and 0.12. Nominal molar ratios for the PAGE-Im polymer were slightly lower, at 0.028, 0.073 and 0.11. The samples were dried *in vacuo* at 60 °C overnight in a vacuum chamber in the glove box (1×10^{-3} Torr) and then at 60 °C for 5 h in a high vacuum oven (4×10^{-8} Torr) to ensure complete removal of solvent. The samples were then transferred into a nitrogen glove box for storage and measurement. The divalent salts caused uneven gelation and precipitation of polymer, requiring further homogenization after drying by pressing the samples between Teflon sheets in a hand press at 90 °C.

Thermal characterization. Standard aluminum DSC pans were loaded with polymer samples in a nitrogen glove box. The samples were briefly exposed to air during the sealing of the pans, then transferred directly into the DSC. The glass transition temperature (T_g) of each sample was measured using a Perkin Elmer DSC 8000 on second heating at 20 °C min^{-1} at the midpoint of the step transition. The T_g of the PAGE and PVMS before functionalization were measured on a TA Instruments Q2000 DSC on second heating at 20 °C min^{-1} using the midpoint method. The T_g of PBD before functionalization was taken from literature.[48] T_g values are shown with error bars of ± 2.5 °C, due to the expected uncertainty of the measurement technique.

Ionic conductivity characterization. Total ionic conductivity was measured as a function of temperature on samples sandwiched between parallel ITO blocking electrodes using electrochemical impedance spectroscopy (EIS). The ITO-coated glass electrodes (Thin Film Devices) were cleaned by sonication for 5 min each in detergent, DI water, acetone and isopropyl alcohol, followed by a 5 min UV/ozone treatment. The electrode thicknesses were measured using a micrometer, after which a double-sided Kapton tape spacer with a 1/8" hole was added to one electrode. Polymer samples were loaded into the hole in the Kapton spacer in a nitrogen glove box. Samples were heated to about 30 °C above their T_g before being sealed with a second ITO electrode. All samples were then heated to 110 °C and pressed in a hand press. The final stack thickness was measured using a micrometer, and the sample thickness was determined by subtracting the electrode thicknesses. EIS was measured with a Biologic SP-200 potentiostat using a sinusoidal 100 mV signal from 1 MHz to 1 Hz at temperatures ranging from 30 °C to 110 °C. The data was converted into dielectric

storage and loss, and the ionic conductivities determined from the real component of conductivity at the maximum in tan(δ).[49] Three samples were measured for each composition, with errors reported as standard deviations from the mean.

Dielectric constant measurement. Dielectric constant measurements were performed using a Biologic VSP-300 and parallel ITO blocking electrodes. ITO electrodes were cleaned as mentioned above. Conductive copper tape was adhered to the back (glass) side of each electrode and silver paste was used to make contact between the front ITO electrode and the copper tape. Two 1 mm by 6 mm double-sided Kapton tape spacers were added to the electrode surface. Dielectric spectra were measured inside a temperature-controlled INSTEC stage with a sinusoidal 100 mV voltage signal from 1 MHz to 100 Hz. For fluid samples (PVMS, PAGE and PBD), the top ITO electrode was sealed first, and the material was then added into the cell inside a nitrogen glove box using capillary action. More viscous samples (PAGE-Im, PBD-Im and PVMS-Im) were spread onto the ITO electrode with Kapton spacers using a spatula, heated on a hot plate inside a nitrogen glove box to allow the sample to flow, and then sealed with another ITO electrode. The static dielectric constant was extracted from the frequency-dependent spectra at a frequency of 1MHz and a temperature of –20 °C, where all samples exhibited a phase of around –90° which indicates a purely capacitive response.

X-ray scattering. Polymer samples were loaded into metal washers in a nitrogen glove box and covered with Kapton tape to prevent moisture uptake during measurement. X-ray scattering measurements were performed as a function of temperature at the National Synchrotron Light Source II (NSLS-II, beamline 11-BM, Brookhaven National Laboratory) with an X-ray energy of 13.5 keV and at the Advanced Light Source (ALS, beamline 7.3.3, Lawrence Berkeley National Laboratory) with an X-ray energy of 10 keV. Samples were equilibrated for 15 min at each temperature before collecting exposures. Data processing, including detector distance calibration using a silver behenate standard, reduction of 2D raw SAXS images into 1D intensity versus q curves and corrections for empty cell scattering were performed using the Nika package for Igor Pro for data taken at the ALS, and using the *SciAnalysis* software for NSLS-II data.[50-51]

Electron Paramagnetic Resonance. Pulse EPR experiments at Q-band (34 GHz) were performed on an ELEXYS 580 Bruker spectrometer equipped with a liquid helium cryostat from Oxford Inc and a 300 W TWT amplifier. Samples were packed into capillaries in a nitrogen glove box, inserted into 3 mm EPR tubes, and sealed with a cap and parafilm to prevent moisture uptake. The samples were quenched from room temperature to 20 K for the EPR measurements; thus the structure surrounding the Cu^{2+} is expected to be representative of the polymers at room temperature.

Electron-spin-echo (ESE) detected EPR. The experiments were carried out with the pulse sequence: $\pi/2$ - τ - π - τ - echo; mw pulse lengths $t_{\pi/2}$ = 16 ns and t_{π} = 32 ns and a τ value of 150 ns were used.

Hyperfine Sublevel Correlation (HYSCORE). The experiments were carried out with the pulse sequence $\pi/2$ - τ - $\pi/2$ - t_1 - π - t_2 - $\pi/2$ - τ - echo. The parameters were: mw pulses of lengths $t_{\pi/2}$ = t_{π} = 16 ns, starting times 40 ns for t_1 and t_2 and incremented by 6 ns. Spectra with a τ value of 150 ns were recorded at 20 K. A shot repetition rate of 1.25 kHz was used and a sixteen-step phase cycle was used to remove unwanted echoes. The time traces of the HYSCORE spectra were baseline corrected with a third-order polynomial, apodized with a Hamming window and zero filled. After two-dimensional Fourier transformation, the absolute value spectra were calculated. EPR and HYSCORE spectra were simulated using the MATLAB Easyspin package using the "saffron" function, with details provided in the SI.[52]

Field-theoretic simulations. Our molecular model for the metal salt-coordinating polymer is constructed out of two species of monomeric beads (denoted A and B), and two small-molecule salt ion species (denoted + and –). The A- and B-type beads have equal statistical segment lengths b and are linked into continuous Gaussian chains with a backbone of species A having degree of polymerization $N_{bb}=100$, with $n_{sc}=19$ equally-spaced symmetric diblock side-chains each with lengths $N_{sc}=2$ and with the B block at the end of the side chain. The charge and bead densities for all species are Gaussian-distributed with a characteristic radius of $a=b/\sqrt{6}$. The short end B-block of the side chains models the pendant imidazole, as indicated in the schematic of this molecular model presented in Figure 2. The dielectric properties of the polymer are incorporated using embedded Drude oscillators; this polarizable-bead approach is amenable to the transformation to a statistical

equilibrium field theory as outlined in previous work by some of us.[53-56] The backbone monomer is granted polarizability volume $\alpha_v^{(A)}$, which is a parameter that we adjust in this study to control the backbone dielectric constant. For monomeric species B (the imidazole), we set $\alpha_v^{(B)} = 0.541\,b^3$; we provide justification for this parameter choice in the Supporting Information. For simplicity, we restrict ourselves to monovalent, unpolarizable salt ions in this work, and fix the background (vacuum) Bjerrum length to $l_b^{(0)} = 32.5\,b$ and the average density of the system to $\rho_0 = 7.35\,b^{-3}$, following previous work.[56] We model the metal-ligand interaction phenomenologically using a Flory interaction parameter $\chi_{B+\dot{c}=-20\dot{c}}$ between species B and the cation—a common approach in models of salt-polymer complexation.[17, 57-58] We also include short-range repulsions for all beads via an excluded volume parameter $\beta u_0 = \rho_0^{-1} = 0.136\,b^3$ which sets a weak system compressibility, and Flory parameters $\chi_{AB}\dot{c}\chi_{\pm\dot{c}=0.2\dot{c}}$ between species A and B, and between the cations and anions (in addition to full electrostatic interactions). Further details on the model and parameter choices are discussed in the SI. Using standard techniques, the field-theoretic canonical partition function takes the form

$$Z = Z_0 \int D[\omega]D\varphi\, e^{-H[[\omega],\varphi]}$$

where the $[\omega]$ is a set of fluctuating chemical potential and pressure fields that mediate the contact (non-electrostatic) interactions, and φ is a fluctuating electrostatic potential field, which mediates the ion-ion, ion-dipole and dipole-dipole interactions in the system.
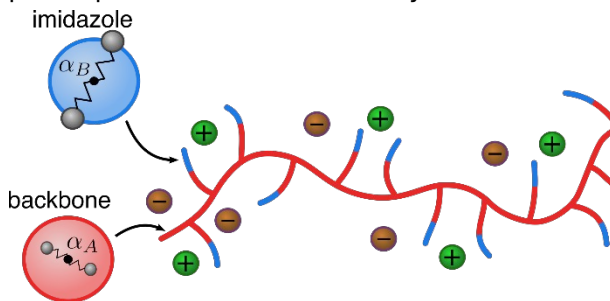

Figure 2. Schematic of the molecular model for the metal salt-coordinating polymer. The backbone monomeric species is shown as red, and the imidazole side chain block is shown as blue, with polarizability volumes α_A and α_B, respectively.

Traditional simplifying (e.g. mean-field) approximations to polymer field theories are typically not appropriate for charged systems due to the importance of electrostatic field fluctuations and charge correlations. Our interest in ion aggregation in this work makes it particularly critical to capture the effect of charge correlations. The complex Langevin sampling technique allows us to perform field-theoretic simulations (FTS) of the model described above without any approximations. The details of the approach are well described in the literature[59-62] and we provide additional specifics regarding our simulations in the Supporting Information.

RESULTS AND DISCUSSION

The goal of this study is to ascertain the impact of polymer backbone polarity on ionic conductivity of both mono and multivalent metal ions. A modular synthetic strategy was employed based on thiol-ene click chemistry which allows the polymer backbone to be altered while keeping the solvating unit, in this case imidazole, constant for all polymers (see Scheme 1). This requires a set of polymer backbones which have pendant vinyl functional handles. Thus, PAGE, 1,2-PBD and PVMS were chosen, as they all have vinyl pendant groups on every monomer. These backbones have varying dielectric constants and T_g's (see Table 1 and Figures S13-S22), both of which are expected to affect salt dissociation and ionic conductivity. The larger molecular weight of the PVMS polymer compared to the PAGE or PBD is not expected to impact the results, since polymer properties such as conductivity and T_g plateau at high molecular weights.[63] PAGE has the highest dielectric constant, at 6.0, while PBD has the lowest dielectric constant at 2.3. Functionalization with the imidazole ligand increases both the dielectric constant and T_g of each polymer, with the largest effect on T_g for the siloxane backbone. We also note that the imidazole-thiol chosen for functionalization incorporates an amide group, which likely plays a role in modifying the dielectric environment and interacting with cations. However, since this functional group combination is present in all polymer samples, its effect is intrinsically included in the experimental measurements.

Scheme 1. Synthesis of imidazole-functionalized polymers proceeds via UV-activated thiol-ene click chemistry in methanol for PAGE or methanol/THF (20/80) mixtures for PVMS and PBD.
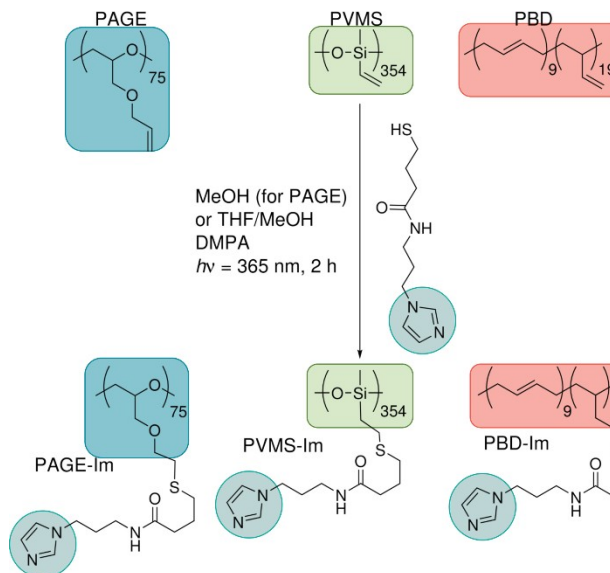
Salt addition increases T_g for all polymer systems as shown in Figure 3. Small amounts of salt result in similar T_g changes for both the monovalent LiTFSI as well as divalent Zn(TFSI)$_2$ and Cu(TFSI)$_2$, while at larger salt concentrations the T_g for the divalent salts increases more significantly than for the monovalent one. This is likely due to the dynamic crosslinking which results upon metal coordination within these polymers.[47] The similar behavior for all three backbone identities suggests metal-ligand interactions

between the pendant imidazole and the salt dominate the T_g trend.[64]

While the T_g behavior is similar for all three polymers, X-ray scattering analysis shows varying amounts of ion clustering or aggregation dependent on the polymer backbone polarity. X-ray scattering profiles taken at 25 °C for a narrow q-range are shown in Figure 4, with the full scattering profiles shown in Figures S23-S25. All three polymer precursors show no correlation peak in the q-range of interest; upon addition of varying concentrations of metal salts a correlation peak appears for all polymers around 0.15 Å^{-1} to 0.3 Å^{-1} (4 nm to 2 nm). These distances are on the same order of magnitude for separation expected for evenly distributed cations/anions at the low salt concentrations probed in this study (see Table S1). However, since the peaks do not shift to higher q (smaller distances) with increasing salt concentration, it is likely that the correlation peak corresponds to spacings between domains of high salt density (i.e. ion aggregation), rather than distances between individual ions. Further evidence for this assignment will be provided with the EPR analysis below. For the PAGE-Im and PVMS-Im polymers, this correlation peak is only visible at a higher salt concentration of $r = 0.12$, while the PBD-Im polymer exhibits ion aggregation even at the lowest salt concentration of $r = 0.03$.

Table 1. Properties of the polymers in this study.

Polymers	Backbone M_n (kDa)	Backbone Đ	Backbone dielectric constant[d]	Functionalized dielectric constant[d]	Backbone T_g (°C)[e]	Functionalized T_g (°C)[e]
PAGE-Im	8.1[a]	1.17[c]	6.0	9.4	–73±2.5	–15±2.5
PVMS-Im	29.5[b]	1.23[c]	2.9	4.7	–115±2.5	–8±2.5
PBD-Im	9.5	1.04	2.3	3.7	–20±2.5 [48]	9±2.5

[a]M_n measured using NMR end-group analysis. [b]M_n measured via GPC with PS standard. [c]Đ measured using GPC with PS standard. [d]Dielectric constants measured at –20 °C at a frequency of 1MHz. [e]T_g measured using DSC upon second heating
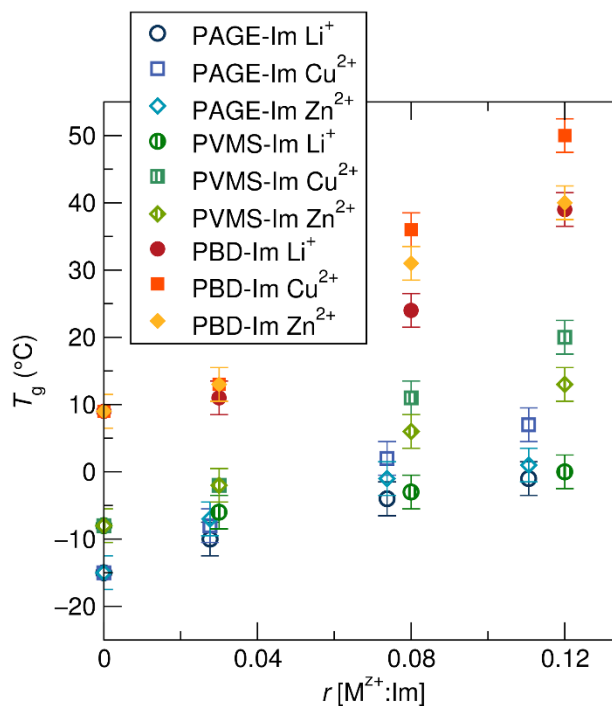
Figure 3. Electrolyte glass transition temperature, T_g, (°C) as a function of salt concentration given in molar ratio of metal cation to imidazole ligand (r) for the three polymer systems studied. T_g increases with salt concentration due to dynamic crosslinking interactions between the polymer and the cations. Error bars show uncertainty of ± 2.5 °C.

The intensity of the peaks changes as a function of both backbone identity and metal salt identity. Zn(TFSI)$_2$-containing samples have the strongest ion aggregation peaks, followed by Cu(TFSI)$_2$. X-ray scattering shows correlation lengths due to differences in electron contrast but does not provide information as to the identity of the species providing that contrast. Thus, it is unclear whether the weaker scattering seen for polymers containing LiTFSI is due to the monovalent nature of Li$^+$, or the much weaker scattering power of Li$^+$ compared to Zn^{2+} and Cu^{2+}. Nevertheless, clear signatures of aggregation in the LiTFSI-containing PBD-Im polymer is observed at a Li$^+$ to imidazole ratio of $r = 0.12$. It is expected that the lower polarity of the PBD backbone in PBD-Im results in the enhanced ion aggregation in this polymer compared with the PVMS or PAGE systems. The effect of temperature on ion aggregation was also probed, showing a slight decrease in peak intensity with increasing temperature as can be seen in Figures S26–S35. This suggests the aggregates become slightly more diffuse as temperature increases, but remain present through the entire temperature range of interest.
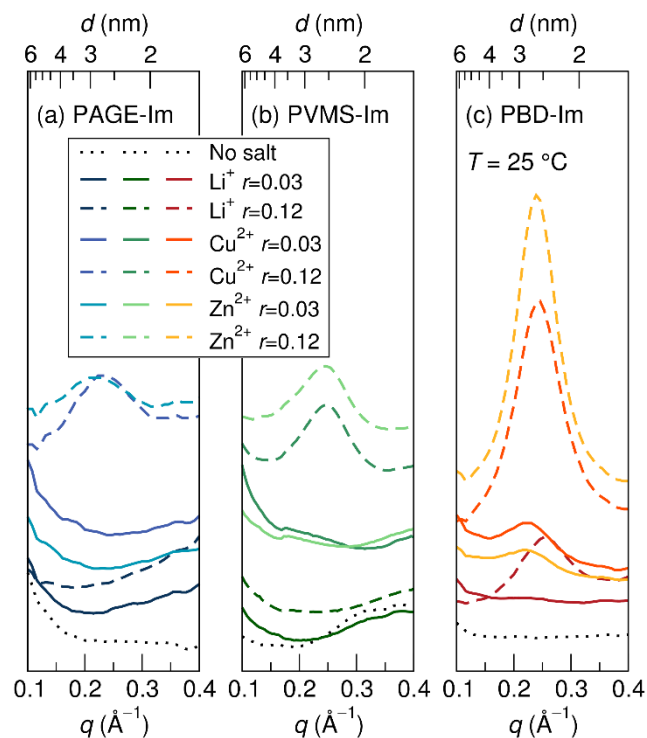
Figure 4. X-ray scattering profiles for the (a) PAGE-Im, (b) PVMS-Im and (c) PBD-Im polymers as a function of salt identity and concentration. Peaks in the scattering profile indicate ion aggregation.

Surprisingly, while the three polymers show dramatic differences in ion aggregation as probed via X-ray scattering, these effects are not manifested in the ionic conductivity behavior. Figure 5 shows the ionic conductivity plotted as a function of salt concentration for all the polymers studied, at a temperature 60 °C above the glass transition temperature for each system. This representation removes effects of changes in T_g with polymer identity, salt identity or salt concentration which were discussed previously (see Figure 3). A temperature of 60 °C above T_g was chosen because this temperature ranged from 49 °C to 110 °C for the various samples, which was directly measurable. Figures S10-11 show the same conductivity trend at relative temperatures of $T – T_g = 30$ and $T – T_g = 90$. Ion aggregation was visible in the X-ray scattering data throughout this temperature range (Figures S26 – S35) No clear trend in conductivity exists as a function of polymer backbone or salt identity. Since the PAGE-Im backbone exhibited the least ion aggregation, especially for the LiTFSI salt, one might have expected the highest conductivities for this system. However, the PBD-Im and PVMS-Im polymers show comparable conductivities for all salts at

7

all concentrations. This suggests that ion aggregation, as measured via X-ray scattering, does not significantly affect conductivity behavior. Instead, as Figure S12 which plots ionic conductivity at an absolute temperature of 60 °C for each system shows, the glass transition temperature is the strongest indicator for conductivity performance in these systems.
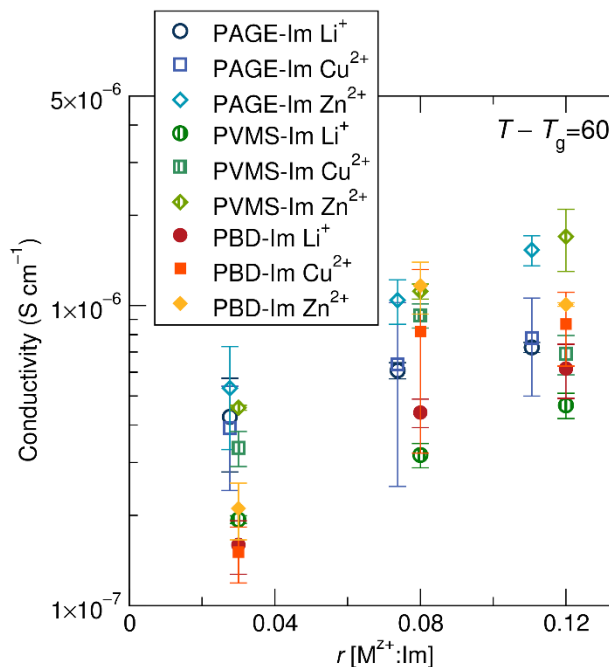

Figure 5. Ionic conductivity is relatively invariant with polymer backbone and salt identity when normalized by the T_g of each system, suggesting ion aggregation plays a minimal role in affecting conductivity.

Understanding how the backbone identity affects the ion aggregate microstructure and ion-ion correlations without significantly impacting ionic conductivity requires us to investigate the nature of the microstructure and correlations in these systems. To this end, we turn to electron paramagnetic resonance (EPR) to probe local ion environments and field-theoretic simulations to identify ion aggregation morphology and characteristics.

While X-ray scattering shows bulk changes in ion aggregation as a function of polymer identity, EPR can be used to identify local changes in the environment of paramagnetic metals. Here, we exploited the EPR properties of Cu^{2+} with an electron configuration of d^9, and hence one unpaired electron in its d-orbital. The copper nucleus itself has two magnetically active isotopes ([63]Cu 69.13 %; [65]Cu 30.83 %) with nuclear spin I = 3/2, thus resulting in hyperfine interactions between the electron and the nuclear spins. The strong spin-orbit coupling and electron-ligand field interactions give rise to significant anisotropy of the g and hyperfine values, both of which are sensitive to the local environment of the Cu^{2+}. Thus, Cu^{2+} was used as a local probe to identify whether the environment around the metal atom is affected by the polymer backbone. Since the largest changes in ion aggregation were observed for the PAGE-Im and PBD-Im polymers, these two systems were chosen for the EPR study. A concentration of $r = 0.03$ was used to probe systems where the ion aggregation as probed via X-ray scattering differed between the two polymers, with the PAGE-Im polymer showing no ion aggregation, but the PBD-Im polymer exhibiting signs of ion aggregation.

Field-Swept Echo (FSE) spectra acquired for PAGE-Im Cu^{2+} and PBD-Im Cu^{2+} at 20 K, shown in Figure 6a, indicate the presence of local ion-ion interactions in both polymers. While the axial Cu^{2+} lineshapes for each of the backbones show subtle differences, both display significant broadening contributions. The spectra show an envelope of the different orientations of the Cu^{2+} spins. Simulation of the lineshape allows us to model the differences in interactions that result from differences in structural nuances between the two backbones (Figure 6b). The EPR parameters extracted from the simulations are summarized in Table 2. The lineshapes for the PBD-Im and PAGE-Im can only be simulated considering a two-component system of i) resolved, isolated, Cu^{2+} ions with an axially elongated tetragonal ligand field ($g_{\parallel} > g_{\perp}$) and ii) a broad, unresolved component, corresponding to clusters of ions, hinting towards ion aggregation even at such low concentrations (Figure S36). The broad component accounts for a significant proportion of EPR active species within the spectrum (~75%) for both polymers. Dipolar coupling is expected to occur in EPR when the Cu^{2+} are within about 1.5 nm from each other.[65-66] A minimum Cu^{2+} concentration for dipolar interaction without aggregation can be calculated, assuming dipolar broadening occurs at separation distances below 15 Å and between evenly-spaced random close packed Cu^{2+} ions. This corresponds to a Cu^{2+} density of around one Cu^{2+} per 170 Å^3 (see SI for calculation). Meanwhile, a molar ratio of $r = 0.03$ as probed here corresponds to a Cu^{2+} concentration of around one Cu^{2+} per 2 nm^3 (see SI for calculation). The contribution of 75% EPR active species to a broadened signal is significantly higher than would be expected from a random distribution of Cu^{2+} ions within the polymer, suggesting that the broad signal indeed comes from aggregated Cu^{2+}. While we are unable to see ion aggregation peaks

8

for such concentrations of Cu^{2+} on the X-ray scattering profiles for the PAGE backbone, X-ray scattering only detects correlations between aggregate clusters rather than between individual ions within an aggregate. In contrast, EPR provides a more sensitive local probe suggesting that multiple Cu^{2+} ions are in close proximity in both backbones, regardless of whether larger scale clustering of ion aggregates occurs or not. Experimentally derived $g_{||}$ and $g_{\perp}$ values listed in Table 2 are typical of Cu^{2+}-imidazole systems, hinting towards binding of the Cu^{2+} and imidazole ligand in both polymers. Strikingly, the hyperfine interactions, both $A_{||}$ and $A_{\perp}$, between the unpaired electron and the copper nuclei are larger than generally observed values for Cu^{2+}-imidazole systems($A_{||}$ = 426 – 615 MHz and $A_{\perp}$ = 39– 50 MHz).[67] The stronger hyperfine interactions suggest greater elongation along both the z-axis and the x-y plane, possibly due to increased steric hindrance from the imidazole tethered to a polymer backbone. The PBD backbone in fact shows even greater hyperfine coupling for both hyperfine components, indicating that the identity of the backbone alters the local environment of the Cu^{2+} metal ion itself. This can be correlated with the backbone's lower polarity, consequently resulting in greater distortion of the environment of the Cu^{2+}, leading to the observance of the ion aggregation peak in the X ray scattering profile.
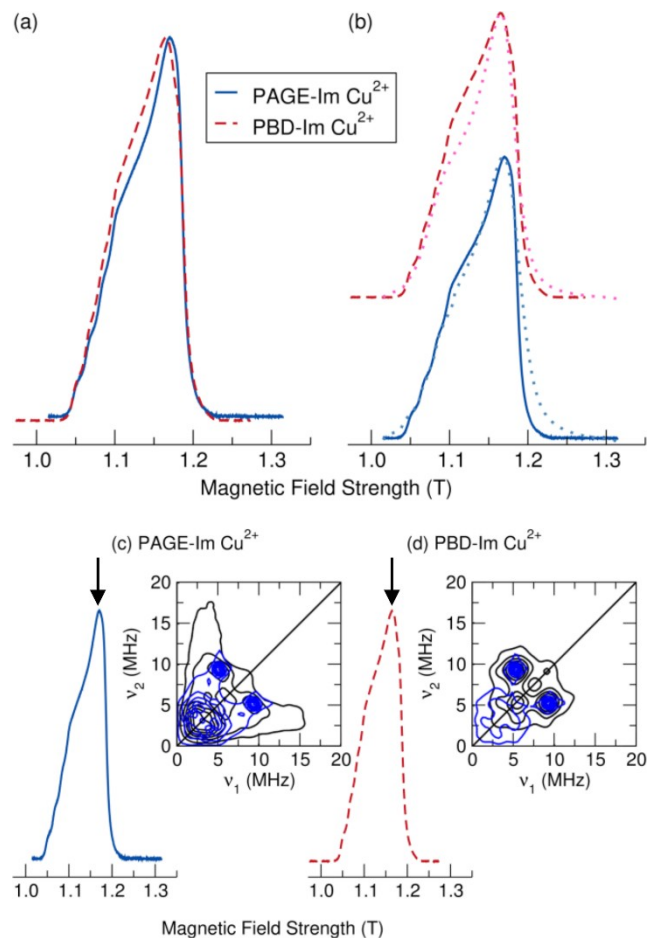
Figure 6. a) FSE of the two polymers with different backbones, recorded at 20 K. b) Comparison of experimental (solid/dashed lines) and simulated spectra (dotted lines) for each polymer. PBD spectra are shifted vertically for clarity. Experimental (black) and simulated (blue) HYSCORE spectra of c) Cu-PAGE-Im and d) Cu-PBD-Im at the maximum observer field position at 20 K.

Table 2. Experimentally derived g and A parameters and contributions from narrow and broad components for both polymer backbones.

	$g_{||}$ (±0.005)	$g_{\perp}$ (±0.005)	$A_{||}$ (±10) (MHz)	$A_{\perp}$ (±10) (MHz)	%
PAGE-Im Cu^{2+} (I)	2.245	2.045	616	112	25
PAGE-Im Cu^{2+} (II)	2.245	2.045	-	-	75
PBD-Im Cu^{2+} (I)	2.250	2.050	686	224	25
PBD-Im Cu^{2+} (II)	2.250	2.050	-	-	75

Lineshape analysis of the Cu^{2+} spectra revealed signatures of the local environment of Cu^{2+}. However, to probe the interactions

between the Cu^{2+} center with the polymer side-chains and the effect of the backbone, we can rely on resolving hyperfine interactions to the ^{14}N nuclei. The question is whether there is differential interaction between Cu^{2+} and ^{14}N when the backbone is altered. In the field-swept echo (FSE) spectra for both polymers, the hyperfine coupling between Cu^{2+} and ^{14}N is hidden within the larger hyperfine interactions between the unpaired electron spins of Cu^{2+} and the ^{63}Cu or ^{65}Cu nuclear spins, and hence not resolved. To closely inspect differences in interaction between Cu^{2+} and imidazole, we used two-dimensional hyperfine sublevel correlation (HYSCORE) spectroscopy, a well-established technique that provides correlations between nuclear frequencies of different spin manifolds that interact with the unpaired electron.[68] The representative HYSCORE spectra collected for the two backbone polymers (Figure 6c,d) show direct interaction of Cu^{2+} and ^{14}N on the imidazole ligand, as expected. The presence of characteristic dq cross-peaks at approximately [5.05 , 9.10] MHz and [9.10, 5.05] MHz in the strong coupling regime ($A>\nu_{14N}/2$) shows direct coordination of ^{14}N species to the unpaired electrons in Cu^{2+} in both polymer backbones. In addition, a broad anisotropic peak appears in the lower frequency regime centered around [3.6, 3.6] MHz for PAGE-Im Cu^{2+}, but not for PDB-Im Cu^{2+}.

Simulations of the HYSCORE data and estimation of the ^{14}N parameters suggest slight differences in Cu^{2+}-imidazole environments between the two backbones. While a single component was successfully fit to the PBD-Im spectra, a second ^{14}N component was required to produce a reasonable fit for the PAGE-Im Cu^{2+} system (Table S2). This second component still corresponds to an imidazole ligand (see SI) but shows slightly less electron delocalization and slightly higher symmetry. Overall, for the PAGE backbone, the EPR analysis suggests that the coordination environment of imidazole bound ligands is more heterogeneous due to the presence of different ^{14}N imidazole species, which coordinate to the Cu^{2+} center differently. We cannot exclude the possibility of an interaction between the Cu^{2+} with the ether oxygens of the backbone in this polymer. ^{16}O has a nuclear spin I=0 and therefore cannot be detected by hyperfine techniques. This would result in a decreased interaction with the imidazole ligand. It should also be noted that cross-suppression of peaks is an effect in HYSCORE, where strongly coupled nuclei can suppress weaker couplings with other nuclei.[69]

In other words, interactions with weakly coupled ^{14}N in the amide linkages of the sidechains may be suppressed due to stronger interactions between Cu^{2+} and the imidazole.

The EPR results suggest both polymer backbones exhibit local Cu^{2+}-Cu^{2+} interactions, but differ in their Cu^{2+}-imidazole interactions. The general similarity in local ion-ion interactions is perhaps surprising given the difference observed in extent of aggregation according to X-ray scattering and in backbone polarity. However, both polymers have generally low dielectric constants and could be expected to promote ion clustering at a local level, as detected by FSE EPR. The HYSCORE data indicates some inhomogeneity of Cu^{2+}-imidazole interactions in the two backbone systems; changes in solvation behavior, which may impact ion screening, might result in more diffuse ion aggregation which is not detected in X-ray scattering because of the breadth of any resulting peak. Importantly, while EPR confirms the presence of ion aggregates in both polymers, it gives no indication of the morphology or connectivity of the ion aggregates, which likely also plays a large role in ionic conductivity behavior.

Field theoretic simulations examine not only the ion-ion correlations but also visualize the ion densities and thus infer structural information directly. Within our statistical field theory approach, we cannot probe instantaneous density configurations, since instantaneous density field operators are complex-valued. Instead, structures are extracted from time-averages over a finite sampling interval for which the averages of the imaginary parts of the field operators have diminished. As discussed in the SI, the choice of sampling interval is a balance between inaccurate structures at too small averaging windows and total loss of structure for too large windows as the full configuration space for the system (including the ion aggregates) is explored.

An examination of the ion-ion correlations in field-theoretic simulations of the model reveals the presence of a correlation peak, a well-known signature of ion aggregation, consistent with both the X-ray scattering and EPR results above. Figure 7 shows the cation-cation structure factor from FTS for a range of salt-loading, and for low and high backbone dielectric constants (referred to as *PBD-Im-like* and *PAGE-Im-like* polymers). A peak in the ion-ion structure factor emerges for high salt-loading ($r>0.026$), significantly stronger for low backbone dielectric constant ($\epsilon=2$) than for high ($\epsilon=10$). No peak is observed for the

10

low salt-loading cases, in agreement with the trends seen via X-ray scattering of the lithium salt-doped systems. The peak in FTS occurs at a wavevector $q^{i} \approx 0.5 a^{-1}$, which may be converted to units of $Å^{-1}$ by estimating the statistical segment length $b \approx 0.5\,nm$ to give $q^{i} \approx 0.25\,Å^{-1}$, in good agreement with the position of the experimentally observed scattering peaks (Figure 8). However, the peak is significantly broader than that seen in the X-ray scattering; we attribute this to the coarse-grained nature of our model, which produces weaker ion-ion correlations due to the soft (Gaussian) nature of the ions.
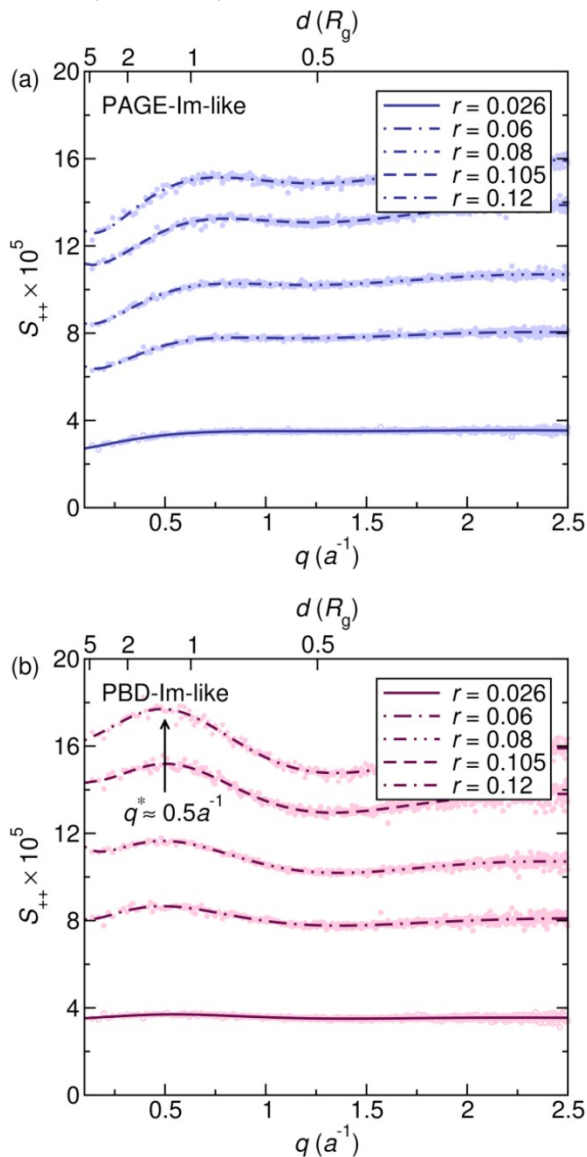
Figure 7. Cation-cation structure factor profiles from simulations of the field-theoretic model, for (a) PAGE-Im-like, and (b) PBD-Im-like polymers for a range of salt concentrations ($r = 0.026 - 0.12$). The points are raw data from field-theoretic simulations, and the lines are visual guides generated via a non-linear curve fit of the raw data.
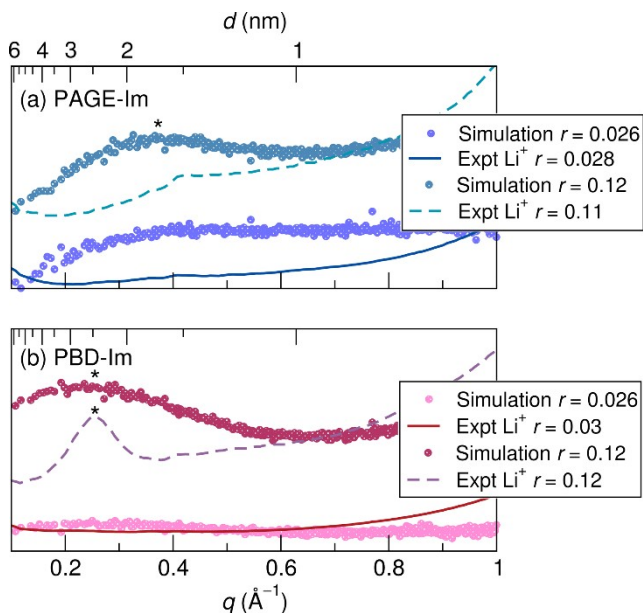
Figure 8. Comparison of experimental X-ray scattering data with FTS cation-cation structure factors for (a) the PAGE-Im polymer and (b) the PBD-Im polymer mixed with LiTFSI. Experimental and simulation data have been scaled vertically for comparison. Peak maxima are indicated by a *.

The cation-cation structure factors in Figure 7 establish that the field-theoretic model exhibits ion correlations that are consistent with the X-ray scattering results, as shown more clearly in Figure 8: the dependence of structure factors on backbone dielectric constant and salt concentration are in qualitative agreement, and the location of the correlation peak is in quantitative agreement for the PBD-Im polymer. The temporally averaged cation densities from field-theoretic simulations are shown in Figure 9(a) for $r = 0.105$, for which the structure factor profiles in Figure 7 indicate significant differences in the extent of ion aggregation for the PAGE-Im-like and PBD-Im-like polymers. Visually, the difference between the cation densities for those cases does not appear to be so great, but the histograms of the cation density reveal a measurable difference. Although for strongly segregated ion channels a bimodal ion density distribution is expected, due to high ion concentration in the ion channels and concomitant low ion concentration in the surrounding matrix, in Figure 9(a) the cation density is distributed *unimodally* for both cases. This indicates that when averaging over the re-arranging ion aggregates, the

11

resulting ion structure can be understood as fluctuations about the bulk ion density, with a characteristic length-scale and a magnitude that depends on the length of the averaging window used. There is a dependence of the magnitude of these fluctuations on the polymer identity (i.e. backbone polarity); that is, the magnitude of the fluctuations is stronger for the PBD-Im-like (low polarity) polymer than for the PAGE-Im-like (high polarity) polymer, as can be seen in the width of the cation density distributions of Figure 9(a). This is a manifestation of the same ion aggregation effects that produce the difference in the structure factors in Figure 7.

$$\phi_+(\mathbf{r}) \geq \langle \phi_+ \rangle$$
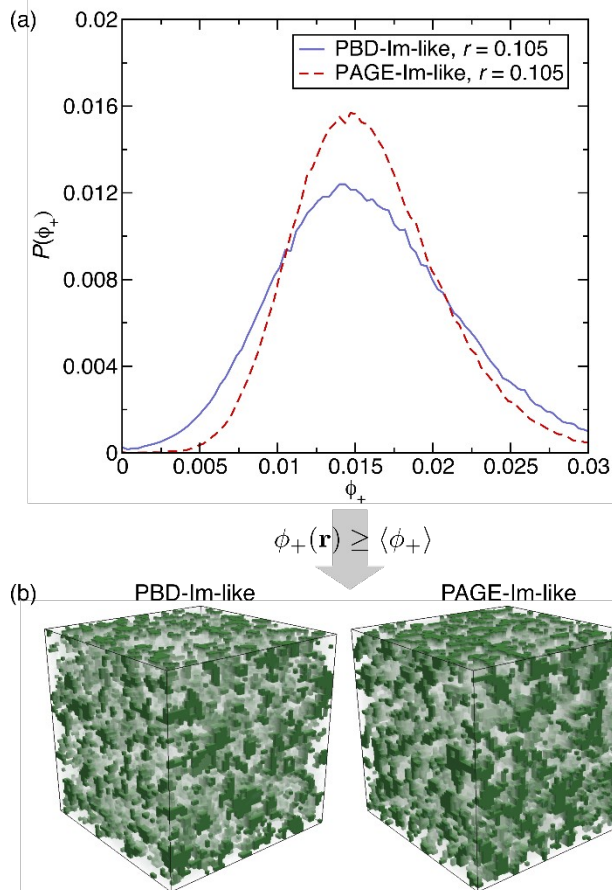
Figure 9. (a) Histograms of the thermally-averaged cation density from FTS for the $r = 0.105$ cases. (b) Ion channels, identified by the criterion $\phi_{+\lfloor(r)\geq\lfloor\lfloor}$, form a percolating network for both polymers.

A rudimentary percolation analysis of the averaged ion morphologies reveals that any differences in the magnitude of the ion density in these channels, due to the difference in polymer backbone polarity, is not sufficient to lead to a substantial difference in their percolation properties. We identify 'ion channels' as those for which the cation

volume fraction $\phi_{+\lfloor(r)\lfloor}$ is greater than its bulk value (in this case, $r = 0.105$ corresponds to $\lfloor$). The resulting channels, which are visualized in Figure 9(b), are analyzed to determine whether or not they percolate through the simulation box. In all directions the channels, as defined by the threshold value $\phi_{+\lfloor\approx0.014\lfloor}$, form a completely percolating network; that is, the ratio of the volume of percolating ion channels to the total volume of ion channels is greater than 0.99. Since the ionic conductivity stems from both cation and anion contributions, it is relevant to confirm that the anion-anion structure factor likewise shows behavior similar to the cation-cation structure factor. Indeed, as can be seen in Figure S40, the anion structure factor and percolation behavior are the same as for the cation.

These results indicate that it is possible for changes in backbone dielectric properties to affect ion aggregation, in a way that would produce differences in the scattering profiles but would *not* produce differences in the percolation properties of the ion channels/network, and thus might not correlate with the ionic conductivity, as was seen in the experimental section of this work.

CONCLUSION

Ionic conductivity in a series of imidazole-tethered graft polymers has been shown to be insensitive to backbone polarity, despite the extent of ion aggregation being greater in the systems with less polar backbones. EPR results reveal that low concentrations of Cu(TFSI)$_2$ in the butadiene and ether-based polymers show similar Cu^{2+}–Cu^{2+} local interactions, indicating that local ion-ion interactions may still be prevalent in all samples even when not visible in X-ray scattering. Field-theoretic simulations suggest ionic aggregates in both the low- and high-dielectric backbone systems are percolated, despite a dependence of the extent of ion aggregation on the backbone dielectric constant, further supporting the similar conductivity performance in these systems when normalized by T_g. These results underscore that ion aggregation is not necessarily detrimental to ionic conductivity, especially in systems where such aggregates form percolating domains with high local mobility. The results emphasize the much larger experimental synthetic space, such as focusing on low T_g and non-interacting backbones, that may be accessible in the search for higher performance ion-conducting polymers, than was previously considered viable.

ASSOCIATED CONTENT

Supporting Information. NMR and GPC molecular characterization, temperature-dependent ionic conductivity and X-ray scattering, dielectric constant measurements, details of HYSCORE simulation, and field-theoretic simulations. This material is available free of charge via the Internet at http://pubs.acs.org.

AUTHOR INFORMATION

Corresponding Authors

* R. A. S.: segalman@ucsb.edu, G. H. F.: ghf@ucsb.edu.

Author Contributions

The manuscript was written through contributions of all authors. All authors have given approval to the final version of the manuscript.

Notes

The authors declare no competing financial interest.

REFERENCES

1. Tarascon, J.-M.; Armand, M., Issues and Challenges Facing Rechargeable Lithium Batteries. *Nature* **2001,** *414*, 359-367.
2. Hallinan, D. T.; Balsara, N. P., Polymer Electrolytes. *Annu. Rev. Mater. Res.* **2013,** *43*, 503-25.
3. Goodenough, J. B.; Kim, Y., Challenges for Rechargeable Li Batteries. *Chem. Mater.* **2010,** *22*, 587-603.
4. Hooper, R.; Lyons, L. J.; Mapes, M. K.; Schumacher, D.; Moline, D. A.; West, R., Highly Conductive Siloxane Polymers. *Macromolecules* **2001,** *34*, 931-936.
5. Wang, Y.; Fan, F.; Agapov, A. L.; Yu, X.; Hong, K.; Mays, J.; Sokolov, A. P., Design of Superionic Polymers—New Insights from Walden Plot Analysis. *Solid State Ionics* **2014,** *262*, 782-784.
6. Webb, M. A.; Jung, Y.; Pesko, D. M.; Savoie, B. M.; Yamamoto, U.; Coates, G. W.; Balsara, N. P.; Wang, Z.-G.; Miller, T. F., Systematic Computational and Experimental Investigation of Lithium-Ion Transport Mechanisms in Polyester-Based Polymer Electrolytes. *ACS Cent. Sci.* **2015,** *1*, 198-205.
7. Khurana, R.; Schaefer, J. L.; Archer, L. A.; Coates, G. W., Suppression of Lithium Dendrite Growth Using Cross-Linked Polyethylene/Poly(ethylene oxide) Electrolytes: A New Approach for Practical Lithium-Metal Polymer Batteries. *J. Am. Chem. Soc.* **2014,** *136*, 7395-7402.
8. Spindler, R.; Shriver, D. F., Investigations of a Siloxane-Based Polymer Electrolyte Employing 13C, 29Si, 7Li, and 23Na Solid-State NMR Spectroscopy. *J. Am. Chem. Soc.* **1988,** *110*, 3036-3043.
9. Johansson, P.; Jacobsson, P., Rational Design of Electrolyte Components by Ab Initio Calculations. *J. Power Sources* **2006,** *153*, 336-344.
10. Webb, M. A.; Savoie, B. M.; Wang, Z.-G.; Miller III, T. F., Chemically Specific Dynamic Bond Percolation Model for Ion Transport in Polymer Electrolytes. *Macromolecules* **2015,** *48*, 7346-7358.
11. Newman, J. S.; Thomas-Alyea, K. E., *Electrochemical systems*. J. Wiley: 2004.
12. Choi, U. H.; Ye, Y.; Salas De La Cruz, D.; Liu, W.; Winey, K. I.; Elabd, Y. A.; Runt, J.; Colby, R. H., Dielectric and Viscoelastic Responses of Imidazolium-Based Ionomers with Different Counterions and Side Chain Lengths. *Macromolecules* **2014,** *47*, 777-790.
13. Barteau, K. P. Poly(Glycidyl Ether)-Based Battery Electrolytes: Correlating Polymer Properties to Ion Transport. University of California, Santa Barbara, 2015.
14. Stacy, E. W.; Gainaru, C. P.; Gobet, M.; Wojnarowska, Z.; Bocharova, V.; Greenbaum, S. G.; Sokolov, A. P., Fundamental Limitations of Ionic Conductivity in Polymerized Ionic Liquids. *Macromolecules* **2018,** *51*, 8637-8645.
15. Diederichsen, K. M.; Fong, K. D.; Terrell, R. C.; Persson, K. A.; McCloskey, B. D., Investigation of Solvent Type and Salt Addition in High Transference Number Nonaqueous Polyelectrolyte Solutions for Lithium Ion Batteries. *Macromolecules* **2018,** *51*, 8761-8771.
16. Mongcopa, K. I. S.; Tyagi, M.; Mailoa, J. P.; Samsonidze, G.; Kozinsky, B.; Mullin, S. A.; Gribble, D. A.; Watanabe, H.; Balsara, N. P., Relationship between Segmental Dynamics Measured by Quasi-Elastic Neutron Scattering and Conductivity in Polymer Electrolytes. *ACS Macro Lett.* **2018,** *7*, 504-508.
17. Ganesan, V.; Pyramitsyn, V.; Bertoni, C.; Shah, M., Mechanisms Underlying Ion Transport in Lamellar Block Copolymer Membranes. *ACS Macro Lett.* **2012,** *1*, 513-518.
18. Ratner, M. A.; Shriver, D. F., Ion Transport in Solvent-Free Polymers. *Chem. Rev.* **1988,** *88*, 109-124.
19. Mindemark, J.; Lacey, M. J.; Bowden, T.; Brandell, D., Beyond PEO—Alternative Host Materials for Li+-Conducting Solid Polymer Electrolytes. *Prog. Polym. Sci.* **2018,** *81*, 114-143.

13

20. Schauser, N. S.; Seshadri, R.; Segalman, R. A., Multivalent Ion Conduction in Solid Polymer Systems. *Mol. Syst. Des. Eng.* **2019,** *4*, 263-279.

21. Johansson, P., First Principles Modelling of Amorphous Polymer Electrolytes: Li+-PEO, Li+-PEI and Li+-PES Complexes. *Polymer* **2001,** *42*, 4367-4373.

22. Torell, L. M.; Jacobsson, P.; Petersen, G., A Raman study of ion solvation and association in polymer electrolytes. *Polym. Advan. Technol.* **1993,** *4*, 152-163.

23. Middleton, L. R.; Winey, K. I., Nanoscale Aggregation in Acid- and Ion-Containing Polymers. *Annu. Rev. Chem. Biomol. Eng.* **2017,** *8*, 499-523.

24. Zardalidis, G.; Pipertzis, A.; Mountrichas, G.; Pispas, S.; Mezger, M.; Floudas, G., Effect of Polymer Architecture on the Ionic Conductivity. Densely Grafted Poly(ethylene oxide) Brushes Doped with LiTf. *Macromolecules* **2016,** *49*, 2679-2687.

25. Ye, Y.; Choi, J.-H.; Winey, K. I.; Elabd, Y. A., Polymerized Ionic Liquid Block and Random Copolymers: Effect of Weak Microphase Separation on Ion Transport. *Macromolecules* **2012,** *45*, 7027-7035.

26. Stowe, M. K.; Liu, P.; Baker, G. L., Star Poly(ethylene oxide) as a Low Temperature Electrolyte and Crystallization Inhibitor. *Chem. Mater.* **2005,** *17*, 6555-6559.

27. Brandell, D.; Priimägi, P.; Kasemägi, H.; Aabloo, A., Branched Polyethylene/Poly(ethylene oxide) as a Host Matrix for Li-ion Battery Electrolytes: A Molecular Dynamics Study. *Electrochim. Acta* **2011,** *57*, 228-236.

28. Wheatle, B. K.; Lynd, N. A.; Ganesan, V., Effect of Polymer Polarity on Ion Transport: A Competition between Ion Aggregation and Polymer Segmental Dynamics. *ACS Macro Lett.* **2018,** *7*, 1149-1154.

29. Wang, W.; Tudryn, G. J.; Colby, R. H.; Winey, K. I., Thermally Driven Ionic Aggregation in Poly(ethylene oxide)-Based Sulfonate Ionomers. *J. Am. Chem. Soc.* **2011,** *133*, 10826-10831.

30. Fragiadakis, D.; Dou, S.; Colby, R. H.; Runt, J., Molecular Mobility and Li+ Conduction in Polyester Copolymer Ionomers based on Poly(ethylene oxide). *J. Chem. Phys.* **2009,** *130*, 064907.

31. O'Reilly, M. V.; Masser, H.; King, D. R.; Painter, P. C.; Colby, R. H.; Winey, K. I.; Runt, J., Ionic Aggregate Dissolution and Conduction in a Plasticized Single-Ion Polymer Conductor. *Polymer* **2015,** *59*, 133-143.

32. Wheatle, B. K.; Keith, J. R.; Mogurampelly, S.; Lynd, N. A.; Ganesan, V., Influence of Dielectric Constant on Ionic Transport in Polyether- Based Electrolytes. *ACS Macro Lett.* **2017,** *6*, 1362-1367.

33. Sinha, K.; Maranas, J., Does Ion Aggregation Impact Polymer Dynamics and Conductivity in PEO-Based Single Ion Conductors? *Macromolecules* **2014,** *47*, 2718-2726.

34. Cheng, Y.; Yang, J.; Hung, J.-H.; Patra, T. K.; Simmons, D. S., Design Rules for Highly Conductive Polymeric Ionic Liquids from Molecular Dynamics Simulations. *Macromolecules* **2018,** *51*, 6630-6644.

35. Chen, Y.; Thorn, M.; Christensen, S.; Versek, C.; Poe, A.; Hayward, R. C.; Tuominen, M. T.; Thayumanavan, S., Enhancement of Anhydrous Proton Transport by Supramolecular Nanochannels in Comb Polymers. *Nat. Chem.* **2010,** *2*, 503-508.

36. Trigg, E. B.; Winey, K. I., Nanoscale Layers in Polymers to Promote Ion Transport. *Mol. Syst. Des. Eng.* **2019,** *4*, 252-262.

37. Zhao, Q.; Shen, C.; Halloran, K. P.; Evans, C. M., Effect of Network Architecture and Linker Polarity on Ion Aggregation and Conductivity in Precise Polymerized Ionic Liquids. *ACS Macro Lett.* **2019,** *8*, 658-663.

38. Abbott, L. J.; Lawson, J. W., Effects of Side Chain Length on Ionic Aggregation and Dynamics in Polymer Single-Ion Conductors. *Macromolecules* **2019,** *52*, 7456-7467.

39. Hall, L. M.; Stevens, M. J.; Frischknecht, A. L., Effect of Polymer Architecture and Ionic Aggregation on the Scattering Peak in Model Ionomers. *Phys. Rev. Lett.* **2011,** *106*, 127801.

40. Hall, L. M.; Seitz, M. E.; Winey, K. I.; Opper, K. L.; Wagener, K. B.; Stevens, M. J.; Frischknecht, A. L., Ionic Aggregate Structure in Ionomer Melts: Effect of Molecular Architecture on Aggregates and the Ionomer Peak. *J. Am. Chem. Soc.* **2012,** *134*, 574-587.

41. Evans, C. M.; Bridges, C. R.; Sanoja, G. E.; Bartels, J.; Segalman, R. A., Role of Tethered Ion Placement on Polymerized Ionic Liquid Structure and Conductivity: Pendant versus Backbone Charge Placement. *ACS Macro Lett.* **2016,** *5*, 925-930.

42. Yakovlev, S.; Wang, X.; Ercius, P.; Balsara, N. P.; Downing, K. H., Direct Imaging of Nanoscale Acidic Clusters in a Polymer Electrolyte Membrane. *J. Am. Chem. Soc.* **2011,** *133*, 20700-20703.

43. Benetatos, N. M.; Chan, C. D.; Winey, K. I., Quantitative Morphology Study of Cu-Neutralized Poly(styrene-ran-methacrylic acid) Ionomers: STEM Imaging, X-ray Scattering, and Real-Space Structural Modeling. *Macromolecules* **2007,** *40*, 1081-1088.

44. Zhou, N. C.; Chan, C. D.; Winey, K. I., Reconciling STEM and X-ray Scattering Data To Determine the Nanoscale Ionic Aggregate Morphology in Sulfonated Polystyrene Ionomers. *Macromolecules* **2008,** *41*, 6134-6140.

45. Buitrago, C. F.; Bolintineanu, D. S.; Seitz, M. E.; Opper, K. L.; Wagener, K. B.; Stevens, M. J.; Frischknecht, A. L.; Winey, K. I., Direct Comparisons of X-ray Scattering and Atomistic Molecular Dynamics Simulations for Precise Acid Copolymers and Ionomers. *Macromolecules* **2015,** *48*, 1210-1220.

46. Lee, B. F.; Kade, M. J.; Chute, J. A.; Gupta, N.; Campos, L. M.; Fredrickson, G. H.; Kramer, E. J.; Lynd, N. A.; Hawker, C. J., Poly(allyl glycidyl ether)-A Versatile and Functional Polyether Platform. *J. Polym. Sci. A: Polym. Chem.* **2011,** *49*, 4498-4504.

47. Sanoja, G. E.; Schauser, N. S.; Bartels, J. M.; Evans, C. M.; Helgeson, M. E.; Seshadri, R.; Segalman, R. A., Ion Transport in Dynamic Polymer Networks Based on Metal-Ligand Coordination: Effect of Crosslinker

Concentration. *Macromolecules* **2018,** *51*, 2017-2026.

48. Roland, C. M.; Casalini, R.; Santangelo, P.; Sekula, M.; Ziolo, J.; Paluch, M. Chemical Structure and Local Segmental Dynamics in 1,2-Polybutadiene. *Macromolecules*. **2003,** *36*, 4954-4959.

49. Runt, J.; Fitzgerald, J. J., Dielectric Spectroscopy of Polymeric Materials: Fundamentals and Applications. American Chemical Society: 1997.

50. Ilavsky, J., *Nika* software for two-dimensional data reduction. *J. Appl. Crystallogr.* **2012,** *45*, 324-328.

51. SciAnalysis. https://github.com/CFN-softbio/SciAnalysis.

52. Stoll, S.; Schweiger, A., EasySpin, a comprehensive software package for spectral simulation and analysis in EPR. *J. Magn. Reson.* **2006,** *178*, 42-55.

53. Martin, J. M.; Li, W.; Delaney, K. T.; Fredrickson, G. H., Statistical Field Theory Description of Inhomogeneous Polarizable Soft Matter. *J. Chem. Phys.* **2016,** *145*, 154104.

54. Grzetic, D. J.; Delaney, K. T.; Fredrickson, G. H., The Effective χ Parameter in Polarizable Polymeric Systems: One-Loop Perturbation Theory and Field-Theoretic Simulations. *J. Chem. Phys.* **2018,** *148*, 204903.

55. Grzetic, D. J.; Delaney, K. T.; Fredrickson, G. H., Contrasting Dielectric Properties of Electrolyte Solutions with Polar and Polarizable Solvents. *Phys. Rev. Lett.* **2019,** *122*, 128007.

56. Grzetic, D. J.; Delaney, K. T.; Fredrickson, G. H., Field-Theoretic Study of Salt-Induced Order and Disorder in a Polarizable Diblock Copolymer. *ACS Macro Lett.* **2019,** *8*, 962-967.

57. Dürr, O.; Dieterich, W.; Nitzan, A., Coupled Ion and Network Dynamics in Polymer Electrolytes: Monte Carlo Study of a Lattice Model. *J. Chem. Phys.* **2004,** *121*, 12732.

58. Qin, J.; de Pablo, J. J., Criticality and Connectivity in Macromolecular Charge Complexation. *Macromolecules* **2016,** *49*, 8789-8800.

59. Fredrickson, G. H., *The Equilibrium Theory of Inhomogeneous Polymers*. Oxford University Press: 2006.

60. Ganesan, V.; Fredrickson, G. H., Field-Theoretic Polymer Simulations. *Europhys. Lett.* **2001,** *55*, 814-820.

61. Düchs, D.; Delaney, K. T.; Fredrickson, G. H., A Multi-Species Exchange Model for Fully Fluctuating Polymer Field Theory Simulations. *J. Chem. Phys.* **2014,** *141*, 174103.

62. Delaney, K. T.; Fredrickson, G. H., Recent Developments in Fully Fluctuating Field-Theoretic Simulations of Polymer Melts and Solutions. *J. Phys. Chem. B* **2016,** *120*, 7615-7634.

63. Shi, J.; Vincent, C. A. The Effect of Molecular Weight on Cation Mobility in Polymer Electrolytes. *Solid State Ionics*. **1993,** *60*, 11-17.

64. Schauser, N. S.; Sanoja, G. E.; Bartels, J. M.; Jain, S. K.; Hu, J. G.; Han, S.; Walker, L. M.; Helgeson, M. E.; Seshadri, R.; Segalman, R. A., Decoupling Bulk Mechanics and Mono- and Multivalent Ion Transport in Polymers Based on Metal–Ligand Coordination. *Chem. Mater.* **2018,** *30*, 5759-5769.

65. Bennet, B.; Antholine, W. E.; D-souza, V. M.; Chen, G.; Ustinyuk, L.; Holz, R. C., Structurally Distinct Active Sites in the Copper(II)-Substituted Aminopeptidases from Aeromonas proteolytica and Escherichia coli. *J. Am. Chem. Soc.* **2002,** *124*, 13025-13034.

66. Richert, S.; Kuprov, I.; Peeks, M. D.; Suturina, E. A.; Cremers, J.; Anderson, H. L.; Timmel, C. R., Quantifying the Exchange Coupling in Linear Copper Porphyrin Oligomers. *Phys. Chem. Chem. Phys.* **2017,** *19*, 16057.

67. Bonomo, R. P.; Riggi, F.; Di Bilio, A. J., EPR Reinvestigation of the Copper (II) -Imidazole System. *Inorg. Chem.* **1988,** *27*, 2510-2512.

68. Shane, J. J.; Höfer, P.; Reijerse, E. J.; de Boer, E., Hyperfine Sublevel Correlation Spectroscopy (HYSCORE) of Disordered Solids. *J. Magn. Reson.* **1992,** *99*, 596-604.

69. Stoll, S.; Calle, C.; Mitrikas, G.; Schweiger, A., Peak Suppression in ESEEM Spectra of Multinuclear Spin Systems. *J. Magn. Reson.* **2005,** *177*, 93-101.

70.

Graphic entry for the Table of Contents (TOC).
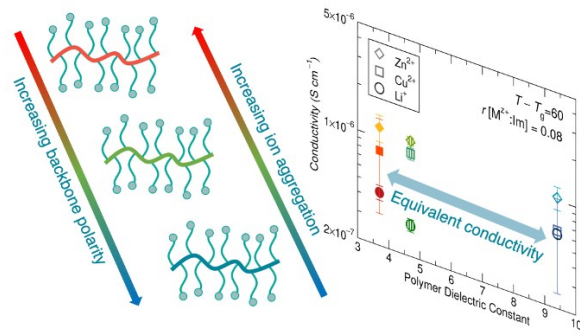
Supporting Information for:

The Role of Backbone Polarity on Aggregation and Conduction of Ions in Polymer Electrolytes

Nicole S. Schauser,[a,b] Douglas J. Grzetic,[b] Tarnuma Tabassum,[c] Gabrielle A. Kliegle,[b,c]

My Linh Le,[d] Ethan M. Susca,[b] Ségolène Antoine,[b] Timothy J. Keller,[c] Kris T. Delaney,[b]

Songi Han,[c] Ram Seshadri,[a,b,c] Glenn H. Fredrickson,[a,b,d,*] Rachel A. Segalman[a,b,d,*]

[a]Materials Department, [b]Materials Research Laboratory, [c]Department of Chemistry and Biochemistry, and [d]Department of Chemical Engineering, University of California, Santa Barbara, California 93106, United States

*Email: ghf@ucsb.edu, segalman@ucsb.edu

Molecular Characterization

NMR and SEC were used for synthesis verification and molecular weight determination. For the PAGE backbone, NMR was used for molecular weight determination based on end group analysis, with 5 protons on the phenyl end group (7.3 ppm) compared with one vinyl proton located at 5.8 ppm (see Figure S1). Functionalization with imidazole was verified by NMR in DMSO-d6 with the disappearance of all vinyl functional character between 5 and 6 ppm for all backbones (see Figures S1, S2 and S3).

$$m = number\ of\ repeat\ units = \frac{I_{phenyl}}{5} * I_{vinyl} = \frac{1.0}{5} * 14.2 = 71$$
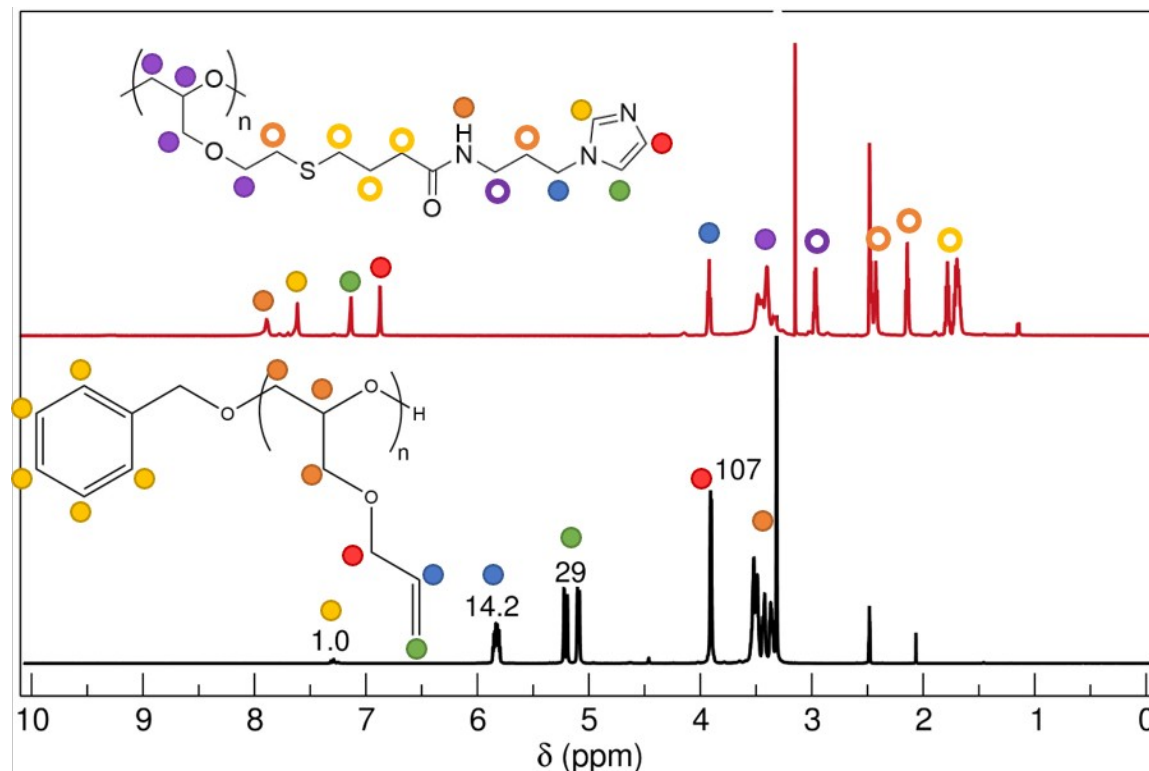
Figure S1. ^{1}H NMR of PAGE (black) and PAGE-Im in DMSO-d6. End group analysis of PAGE suggests 71 repeat units per chain. The disappearance of vinyl character suggests full functionalization for PAGE-Im.
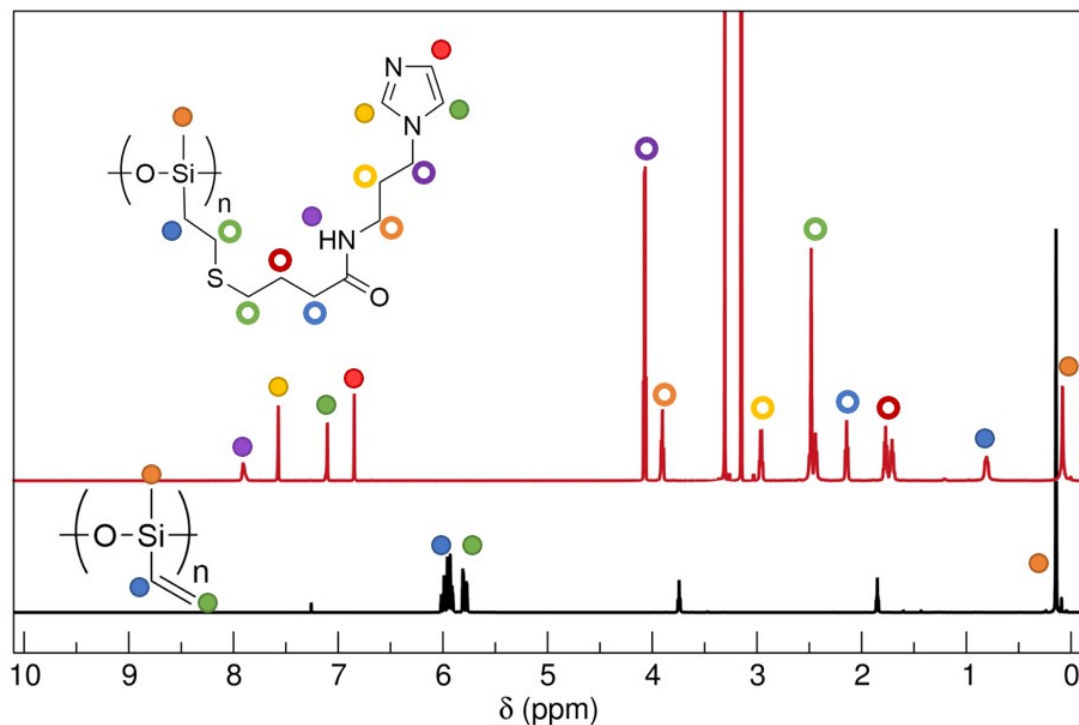
Figure S2. ^{1}H NMR of PVMS in CDCl$_3$ (black) and PVMS-Im in DMSO-d6 (red) showing the disappearance of vinyl character upon functionalization and the appearance of the aromatic imidazole peaks between 6.5 and 8 ppm.
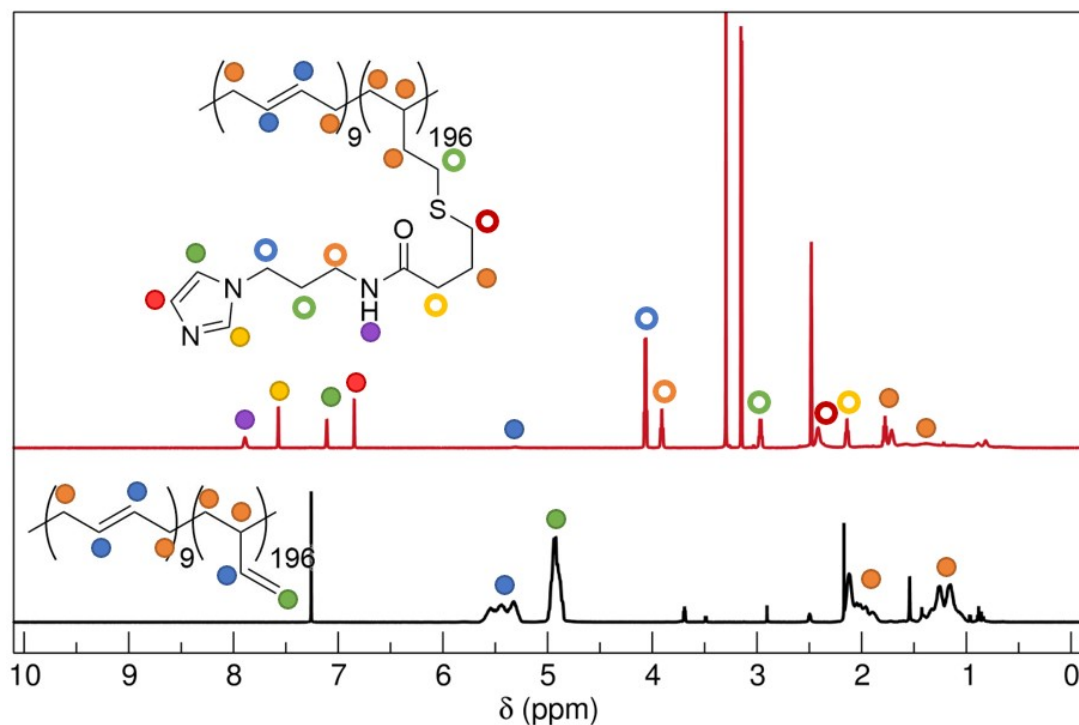
Figure S3. ^{1}H NMR of PBD in CDCl$_3$ (black) and PBD-Im in DMSO-d6 (red), showing the disappearance of vinyl character (4.7-5.7 ppm) upon functionalization.

19
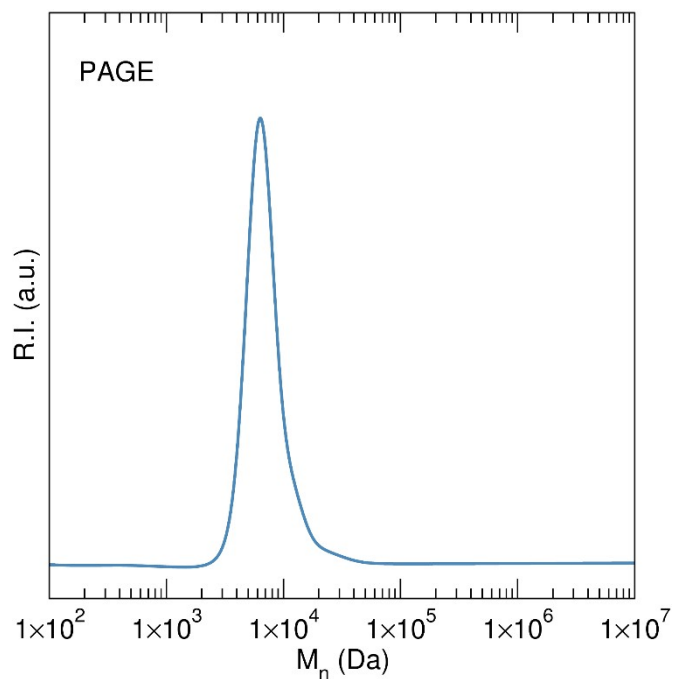
Figure S4. SEC trace of PAGE calibrated against polystyrene standards. The polydispersity was below 1.2, with M_n = 7.3kDa.
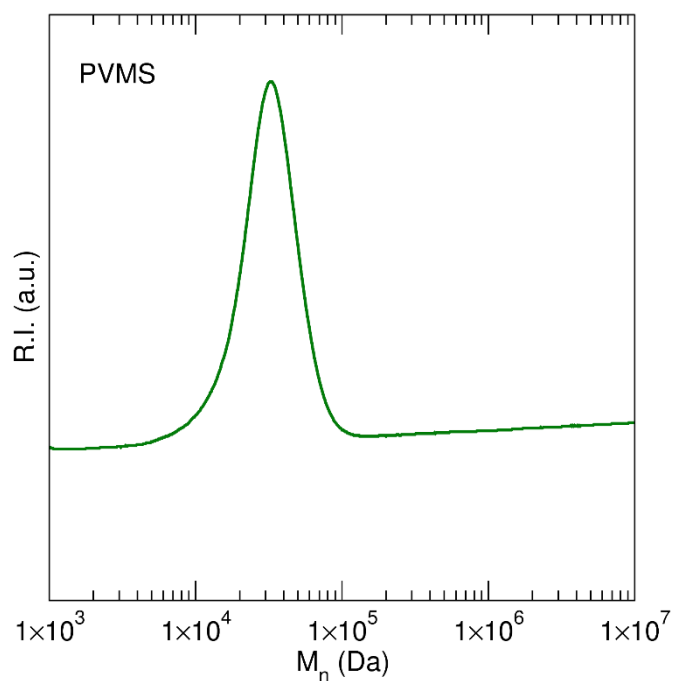
Figure S5. SEC trace of PVMS calibrated against polystyrene standards. The polydispersity was below 1.25, with M_n = 29.5kDa.

Ionic Conductivity

20

All conductivity samples were measured as a function of temperature and fit to VFT formalism as $\sigma = A\exp\left(\dfrac{-B}{T-T_g+50}\right)$. A representative conductivity plot is shown in Figure S6 for PAGE-Im with Cu(TFSI)$_2$ at a molar ratio of 0.08.
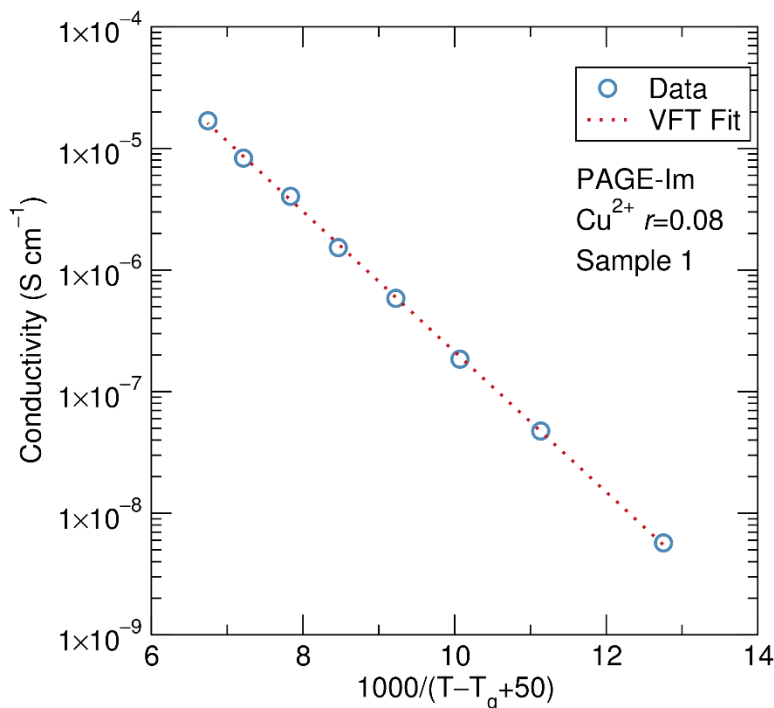
Figure S6. Ionic conductivity versus temperature adjusted by the VFT formalism for a representative sample, PAGE-Im with Cu(TFSI)$_2$ at a metal to imidazole ratio of 0.08. The VFT fit to the data is shown in the dotted line.
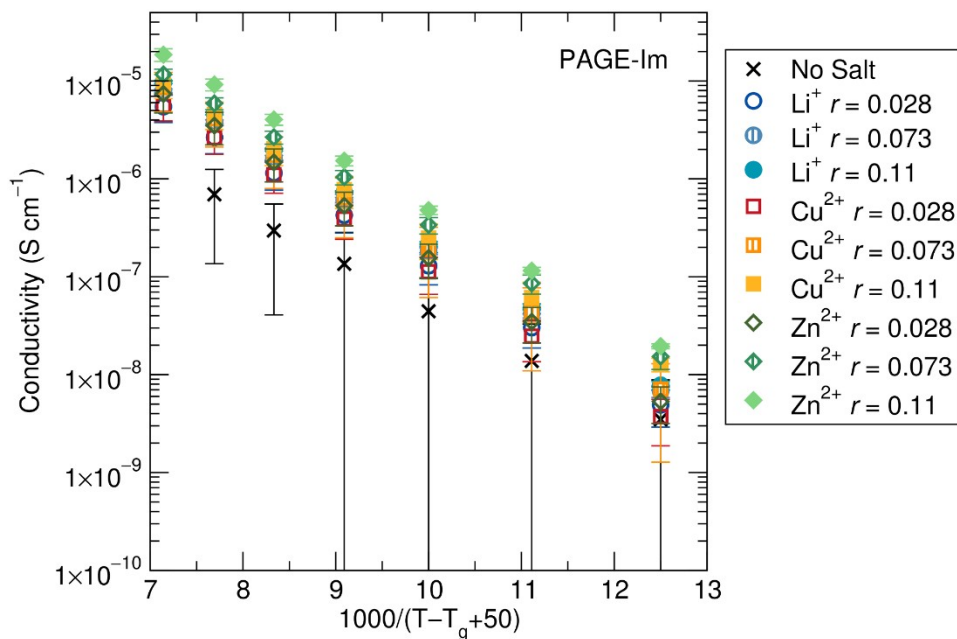
Figure S7. Average ionic conductivity versus temperature for PAGE-Im polymers. Error bars show standard deviation.

21
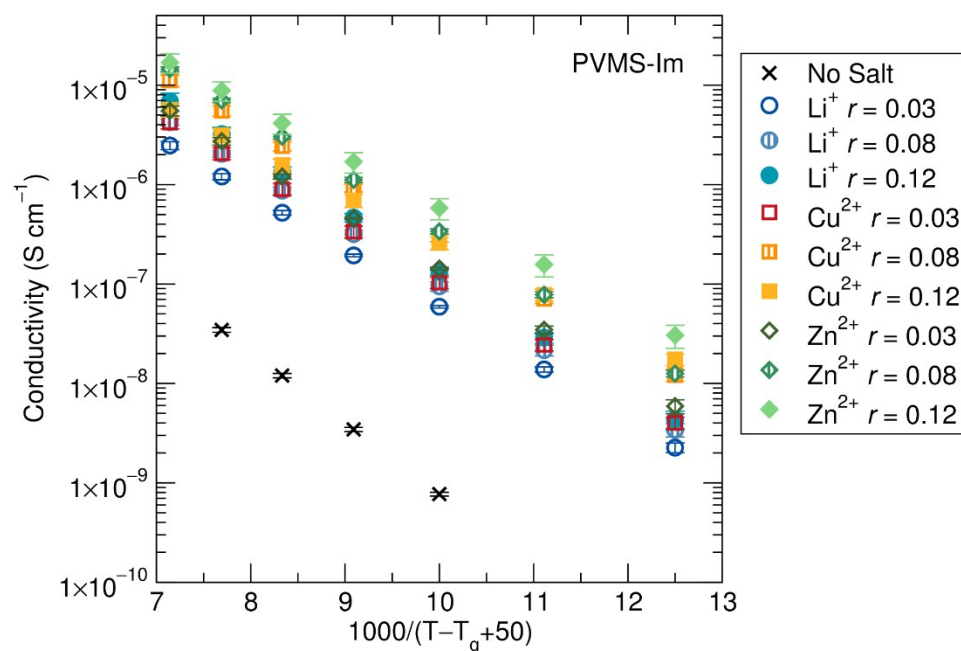
Figure S8. Average ionic conductivity versus temperature for PVMS-Im polymers. Error bars show standard deviation.
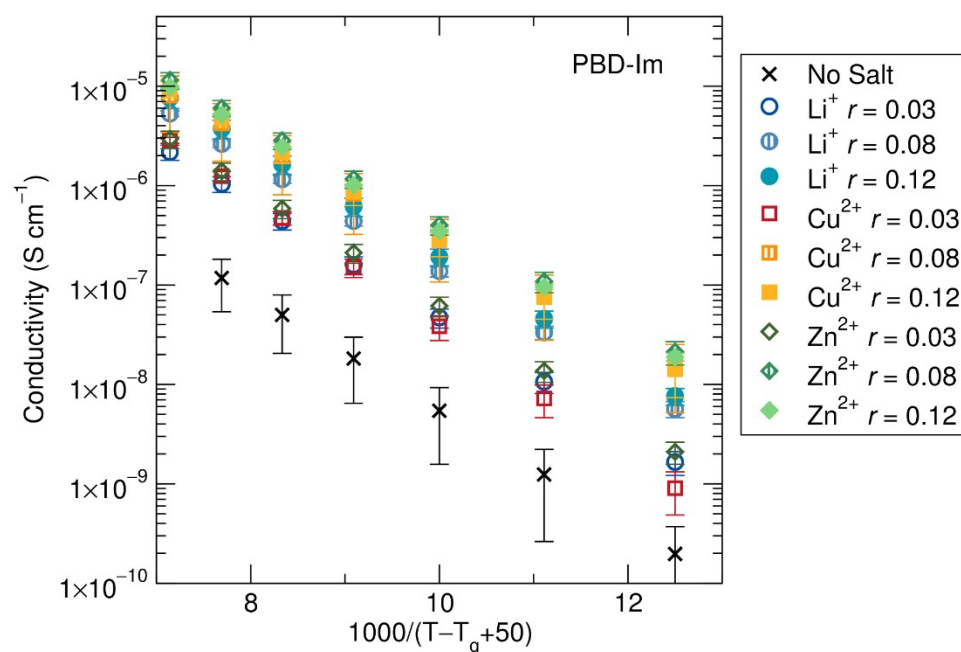
Figure S9. Average ionic conductivity versus temperature for PBD-Im polymers. Error bars show standard deviation.
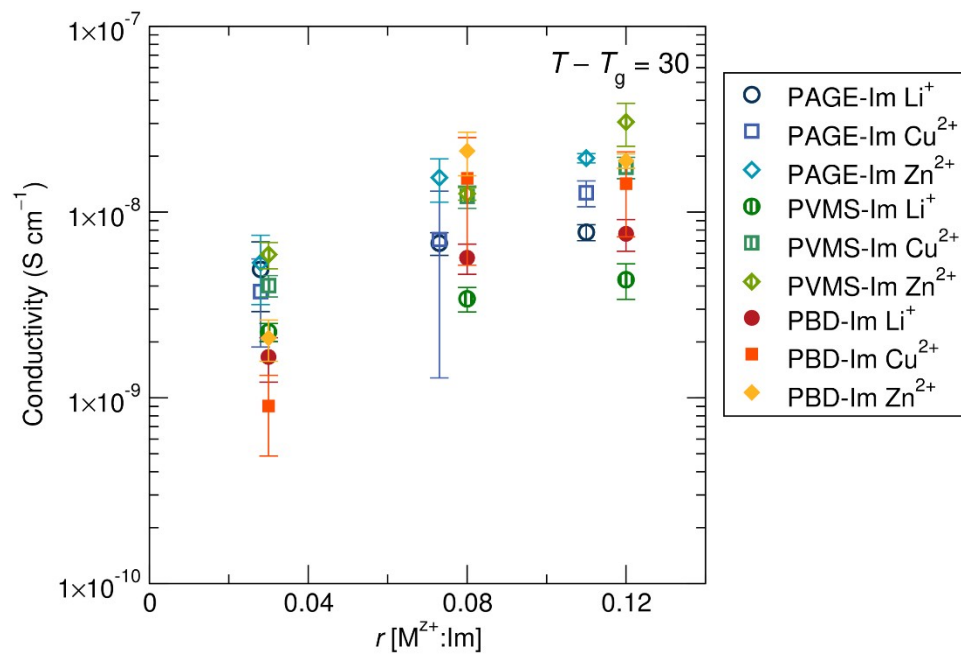
Figure S10. Ionic conductivity at T–T_g = 30 versus salt concentration.
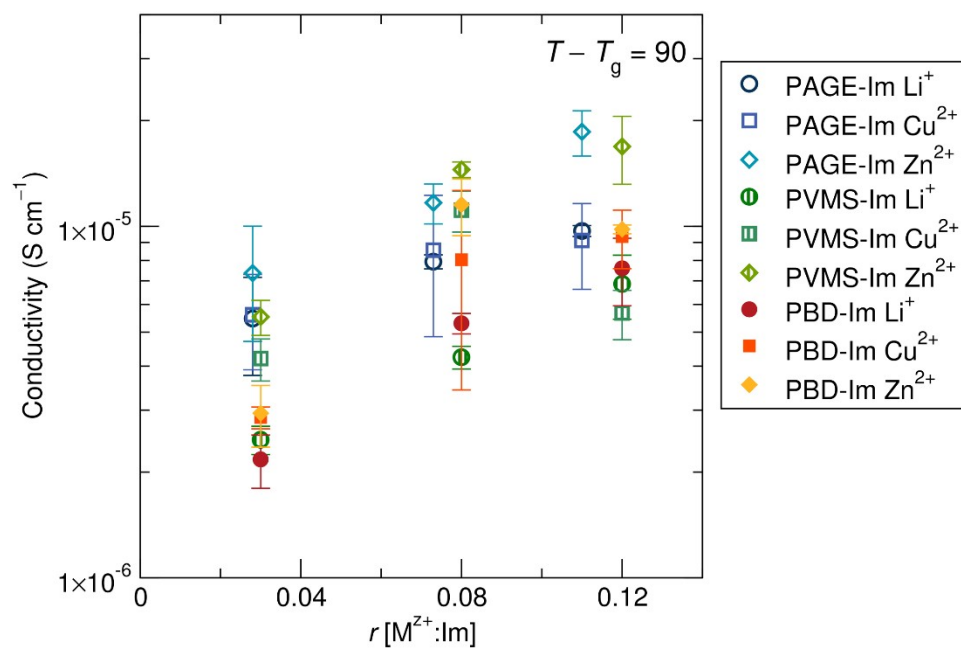
Figure S11. Ionic conductivity at T–T_g = 90 versus salt concentration.
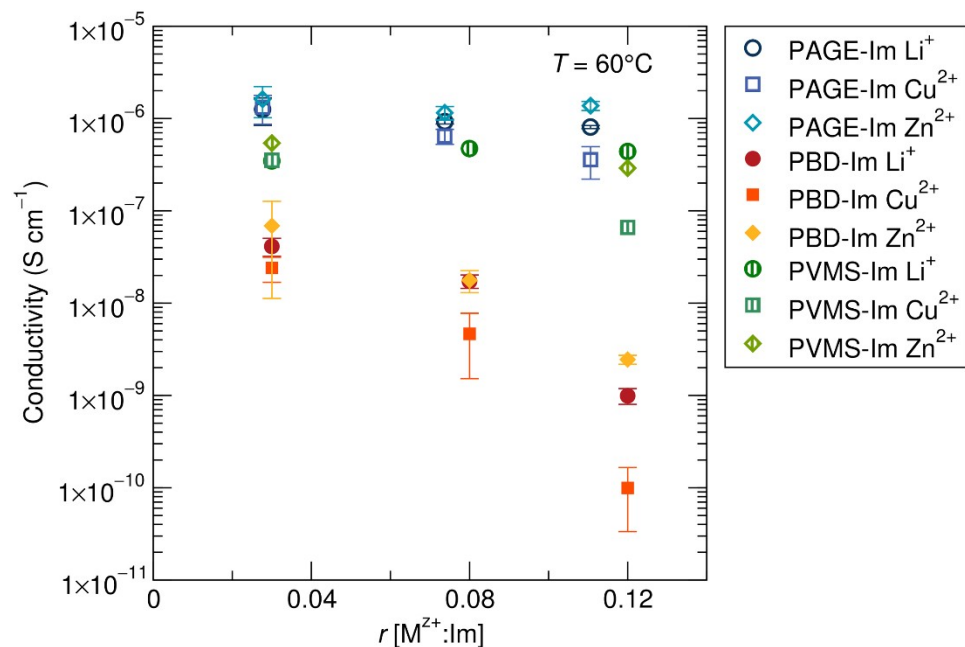
Figure S12. Ionic conductivity as a function of salt content at a constant temperature of 60 °C. Conductivity decreases with increasing salt content due to an increase in T_g. This is especially stark for the PBD backbone due to the proximity to T_g, which reaches 50 °C for the PBD-Im Cu^{2+} r = 0.12 sample.

DSC Measurement

All plots are shown upon second heating, endo up.
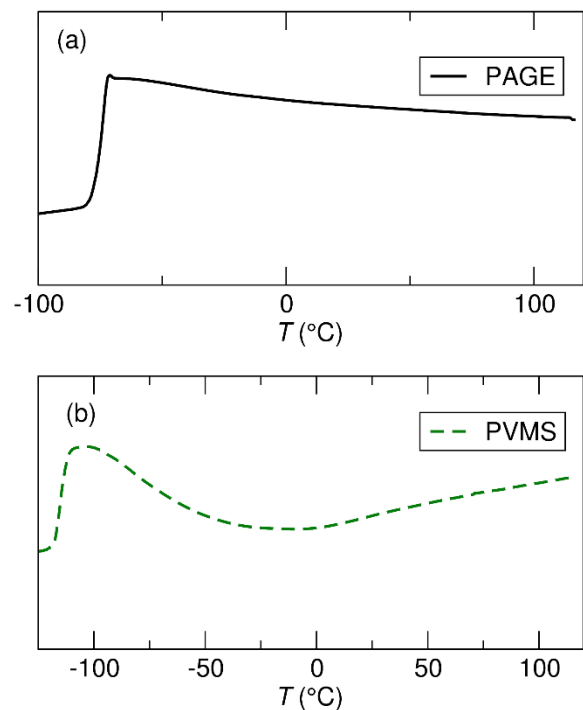
Figure S13. DSC data upon second heating of (a) PAGE and (b) PVMS before functionalization.
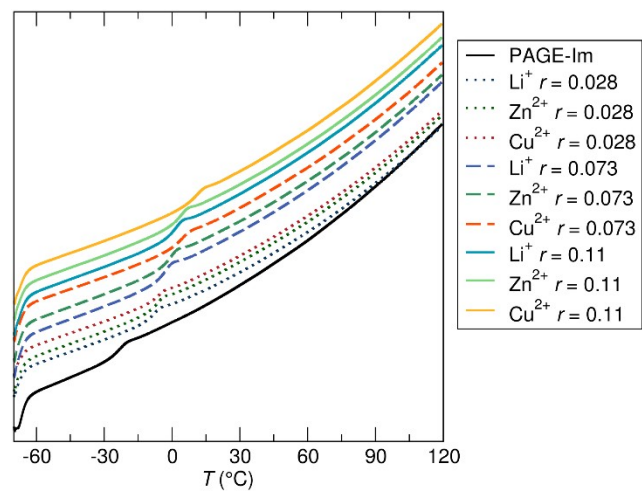
Figure S14. DSC data upon second heating of PAGE-Im with and without salt showing the shift in T_g with salt identity and concentration.
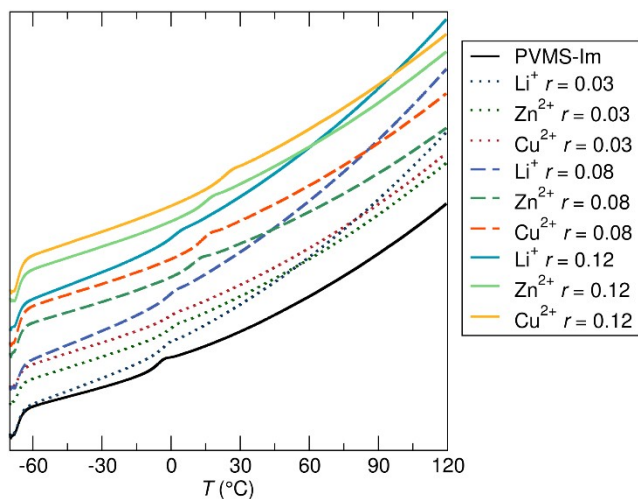
Figure S15. DSC data upon second heating of PVMS-Im with and without salt showing the shift in T_g with salt identity and concentration.
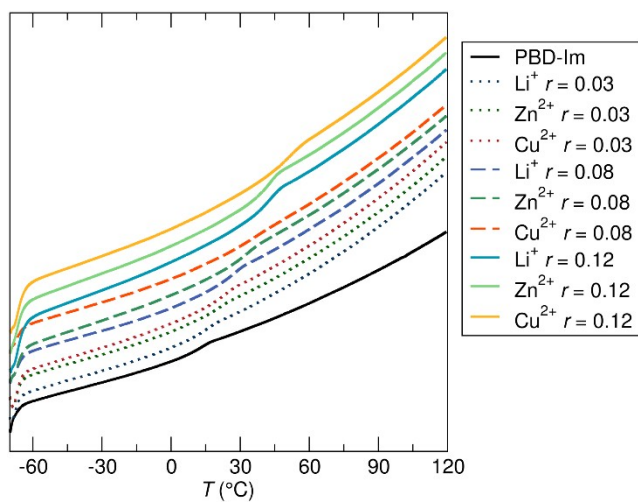
Figure S16. DSC data upon second heating of PBD-Im with and without salt showing the shift in T_g with salt identity and concentration.

Dielectric Constant Measurement

26

Dielectric constants were measured at – 20 °C to minimize the onset of polarization which would lead to an overestimation of the dielectric constant. PAGE, PVMS and PBD were measured before and after functionalization, as shown in Figures S17 through S22. The dielectric constant is calculated from the sample capacitance divided by the cell constant, $C_0 = \dfrac{\varepsilon_0 A}{t}$. While reproducible noise is present in all samples, the value of the dielectric constant does not change significantly.
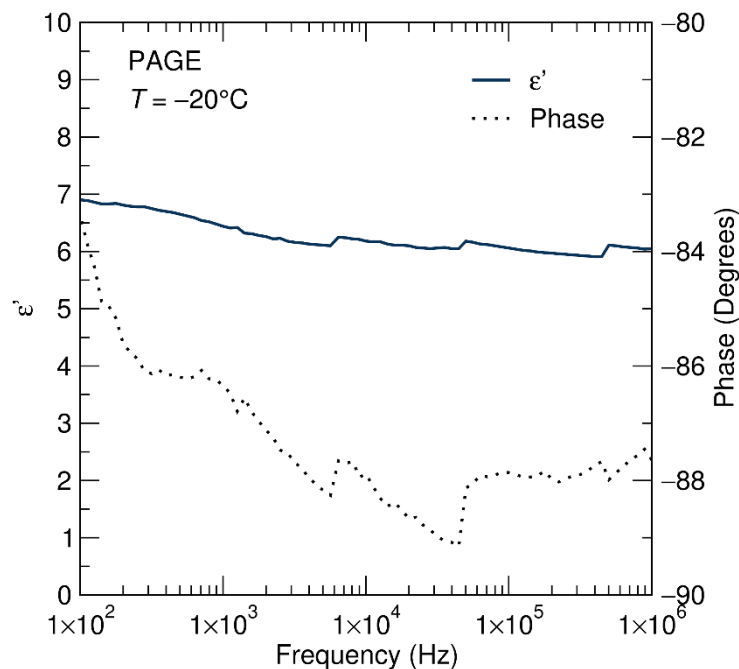
Figure S17. Dielectric constant and phase as a function of frequency for PAGE at –20 °C. Dielectric constants in Table 1 are reported at 1 MHz.
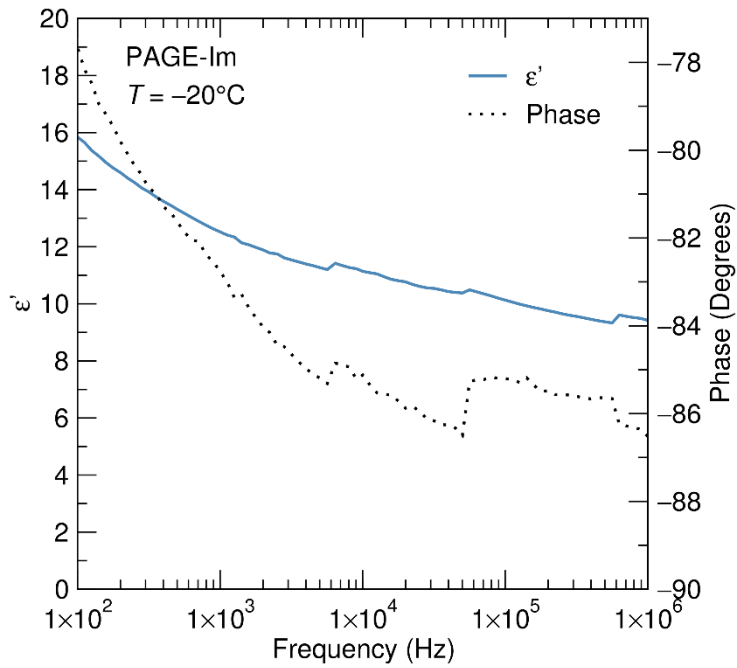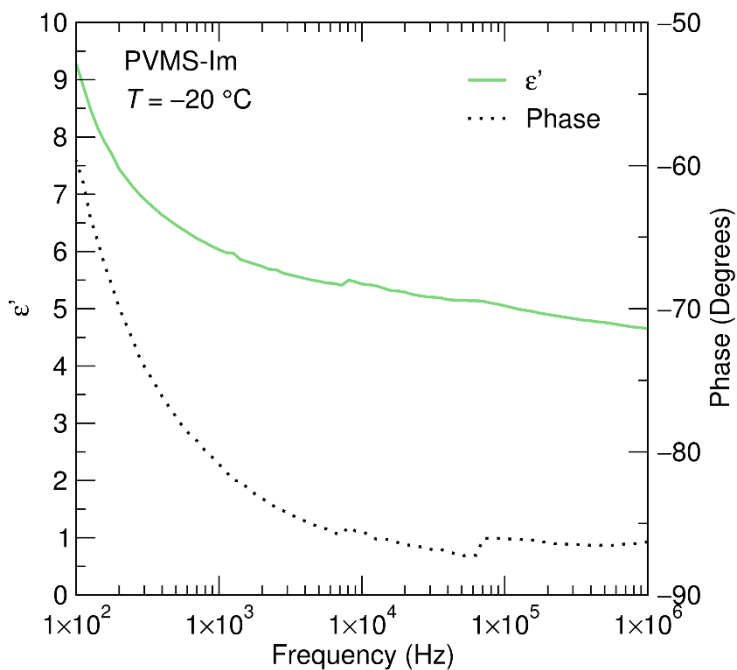
Figure S18. Dielectric constant and phase as a function of frequency for PAGE-Im at –20 °C. Dielectric constants in Table 1 are reported at 1 MHz.
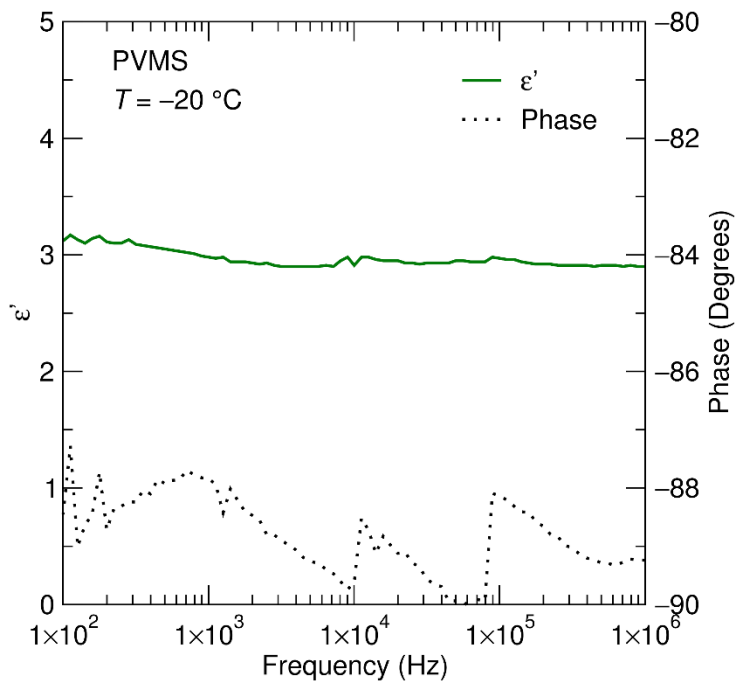
Figure S19. Dielectric constant and phase as a function of frequency for PVMS at –20 °C. Dielectric constants in Table 1 are reported at 1 MHz.
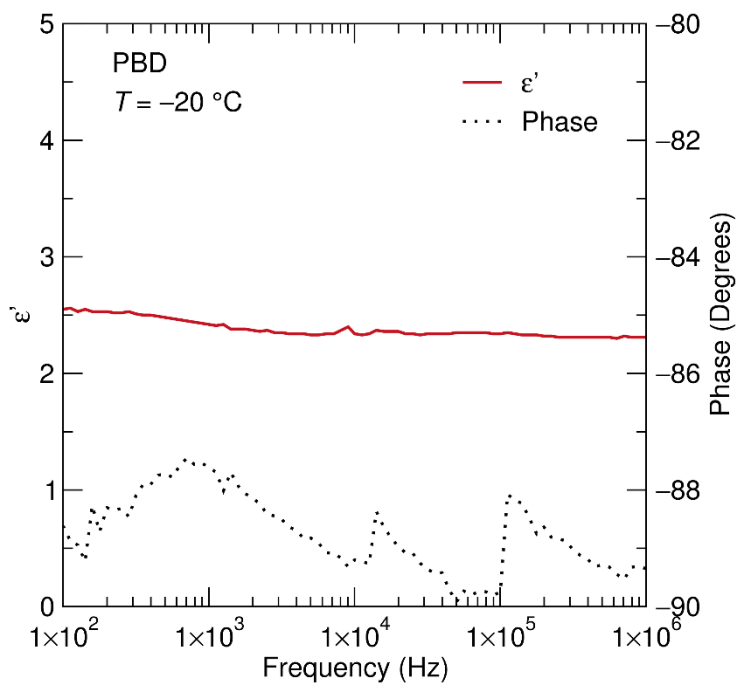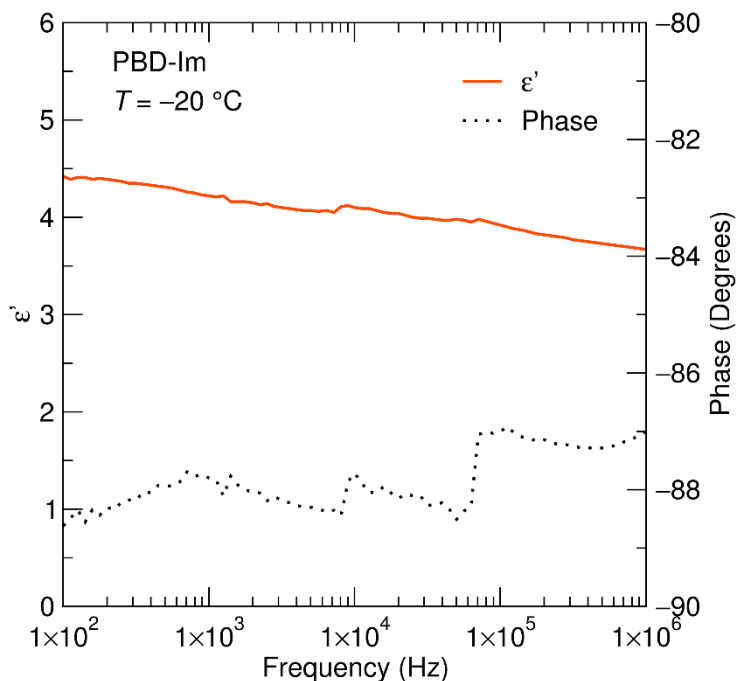
28

Figure S20. Dielectric constant and phase as a function of frequency for PVMS-Im at –20 °C. Dielectric constants in Table 1 are reported at 1 MHz.

Figure S21. Dielectric constant and phase as a function of frequency for PBD at –20 °C. Dielectric constants in Table 1 are reported at 1 MHz.

Figure S22. Dielectric constant and phase as a function of frequency for PBD-Im at –20 °C. Dielectric constants in Table 1 are reported at 1 MHz.

X-ray Scattering Characterization

Separation distance for evenly dispersed ions

For a molar ratio of Li$^+$, Cu^{2+}, or Zn^{2+} to imidazole of $r = 0.03$, and assuming a polymer density of around 1g×cm^{-3}, and a monomer molar mass of 341.5 g/mol (PAGE-Im), we calculate a concentration of M^{z+} in the polymer as follows:

$$\frac{1\,g}{cm^3} \times \frac{cm^3}{10^{24}\,\mathring{A}^3} \times \frac{1\,mol\,polymer}{341.5\,g} \times \frac{1\,mol\,imidazole}{1\,mol\,polymer} \times 0.03\,mol\,\frac{M^{z+\lower.5ex\hbox{$\scriptstyle¿$}}}{1\,mol\,imidazole} \times \frac{6.02 \times 10^{23}\,ions}{1\,mol\,M^{z+\lower.5ex\hbox{$\scriptstyle¿$}}\,¿}$$

$$¿0.00005\,\frac{M^{z+\lower.5ex\hbox{$\scriptstyle¿$}}}{\mathring{A}^3} = 0.05\,\frac{M^{z+\lower.5ex\hbox{$\scriptstyle¿$}}}{nm^3}\,¿¿$$

This corresponds to one metal ion in 20 nm^3, or an average separation distance of 20$^{1/3}$ nm or 2.7 nm. A similar calculation can be performed for the other salt concentrations and polymers, with the results listed in Table S1 below.

Table S1. Approximate cation separation distances expected for evenly dispersed ions for the three polymers and three concentrations studied.

Polymer	$r = 0.03$	$r = 0.08$	$r = 0.12$
PAGE-Im	2.7 nm	1.9 nm	1.7 nm
PVMS-Im	2.6 nm	1.9 nm	1.6 nm
PBD-Im	2.5 nm	1.8 nm	1.6 nm

Below we show the circular averages for the various polymers, salts and concentrations probed in this study. Figures S26 – S35 show the scattering profiles as a function of temperature for those samples that showed aggregation peaks; for those samples which did not show any aggregation, this did not change with elevated temperature.
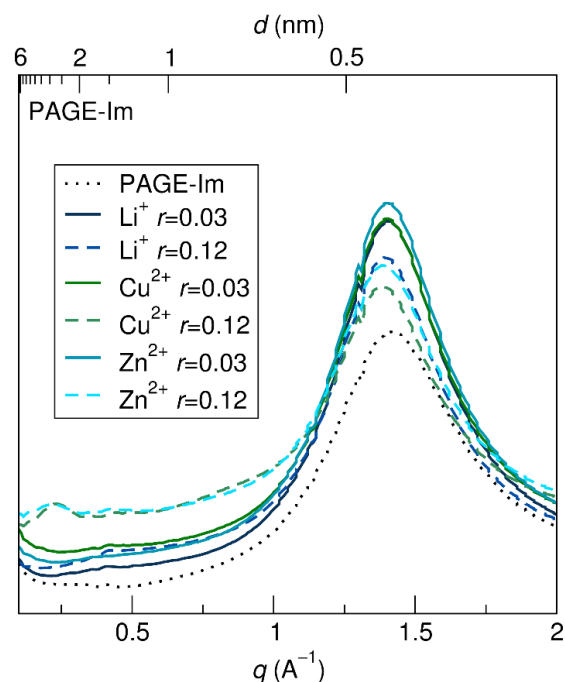

Figure S23. X-ray scattering profile for PAGE-Im at 25 °C with varying salt identities and concentrations, showing a small aggregation peak around 0.22 $Å^{-1}$ and an amorphous halo around 1.4 $Å^{-1}$.
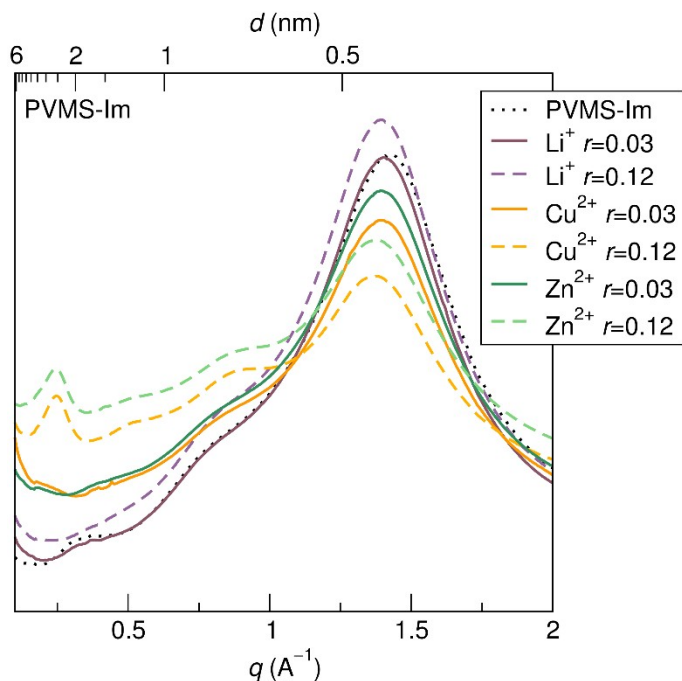
Figure S24. X-ray scattering profile for PVMS-Im at 25 °C with varying salt identities and concentrations, showing an aggregation peak between 0.15 and 0.25 Å^{-1} and an amorphous halo around 1.4 Å^{-1}.
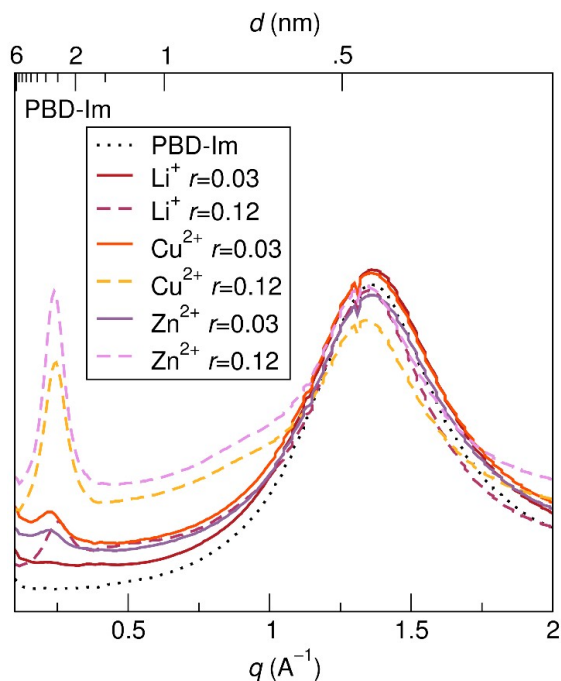

Figure S25. X-ray scattering profile for PBD-Im at 25 °C with varying salt identities and concentrations, showing an aggregation peak between 0.2 and 0.3 Å^{-1} and an amorphous halo around 1.4 Å^{-1}.
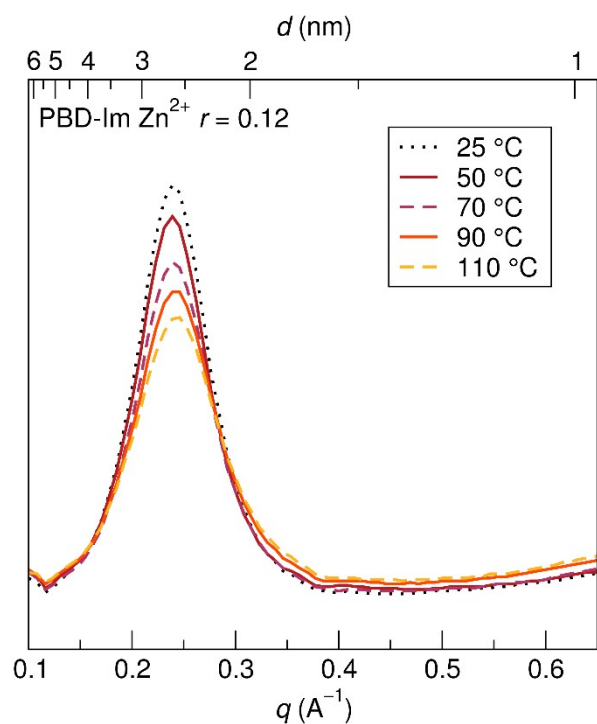
Figure S26. X-ray scattering profile for PBD-Im Zn(TFSI)$_2$ with a molar ratio of Zn^{2+}:imidazole of 0.12 as a function of temperature shows a reduction in the intensity of the correlation peak centered around 0.24 Å^{-1}. This behavior is representative of all samples showing aggregation probed as a function of temperature.
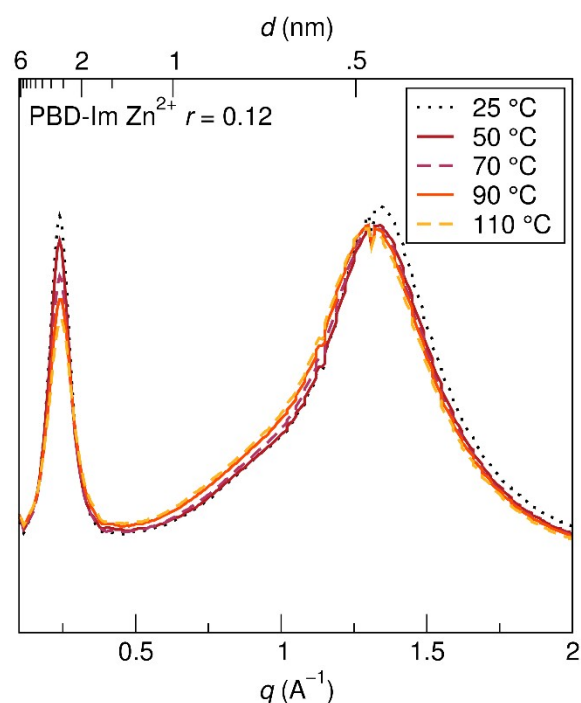

Figure S27. The full X-ray scattering profile for the sample PBD-Im Zn^{2+} $r =$ 0.12 sample shown in Figure S26.
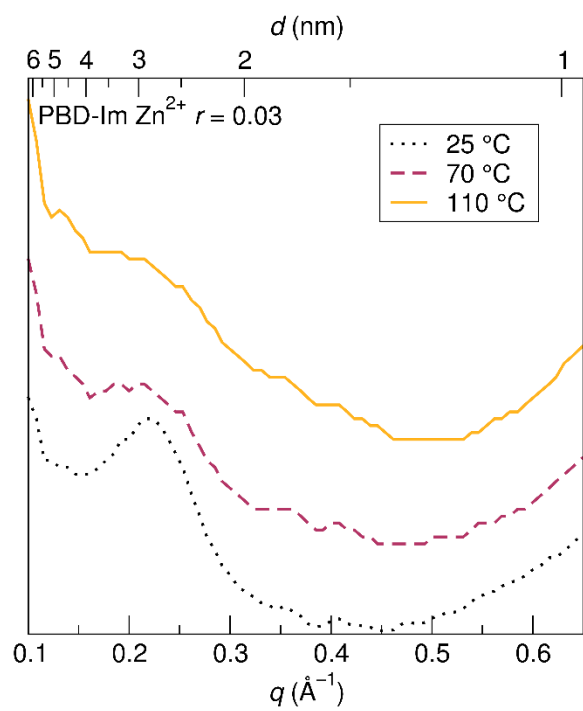
Figure S28. X-ray scattering at 25 °C, 70 °C, and 110 °C for PBD-Im Zn^{2+} r = 0.03. The scattering peak diminishes in intensity at elevated temperatures.

Figure S29. X-ray scattering at 25 °C, 70 °C, and 110 °C for for PBD-Im Li^+ r = 0.12.

34

Figure S30. X-ray scattering at 25 °C, 70 °C, and 110 °C for for PBD-Im Cu^{2+} r = 0.12.

Figure S31. X-ray scattering at 25 °C, 70 °C, and 110 °C for for PBD-Im Cu^{2+} r = 0.03. The scattering peak diminishes in intensity at elevated temperatures.
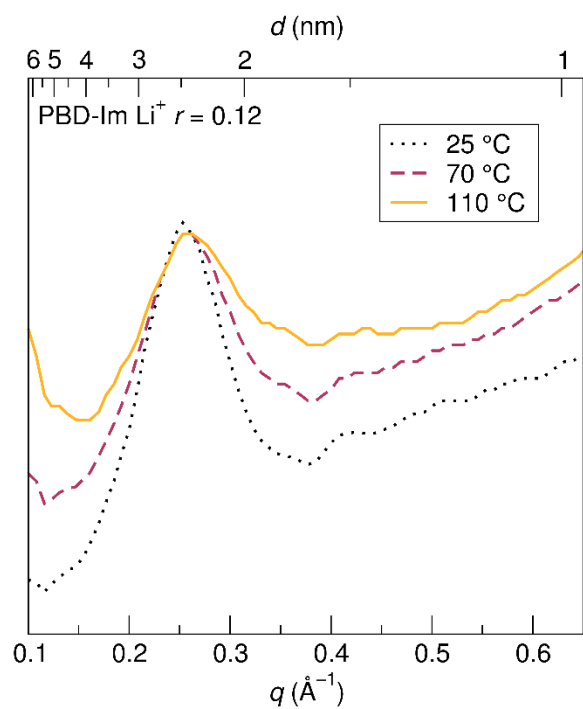
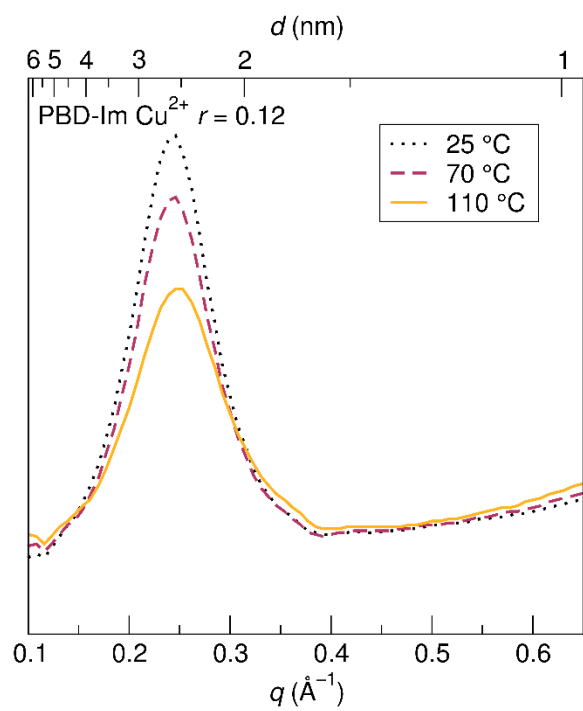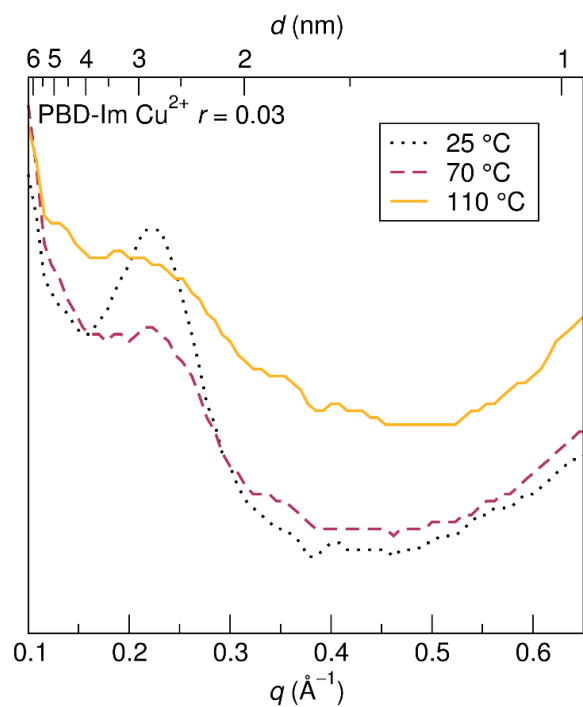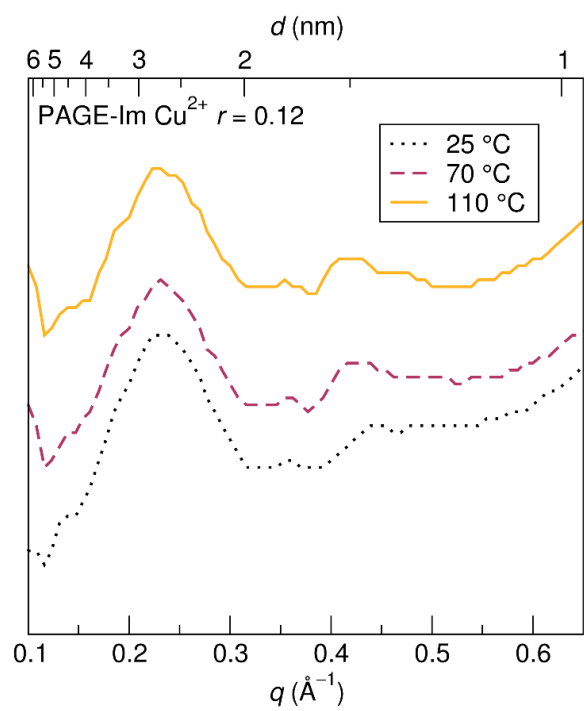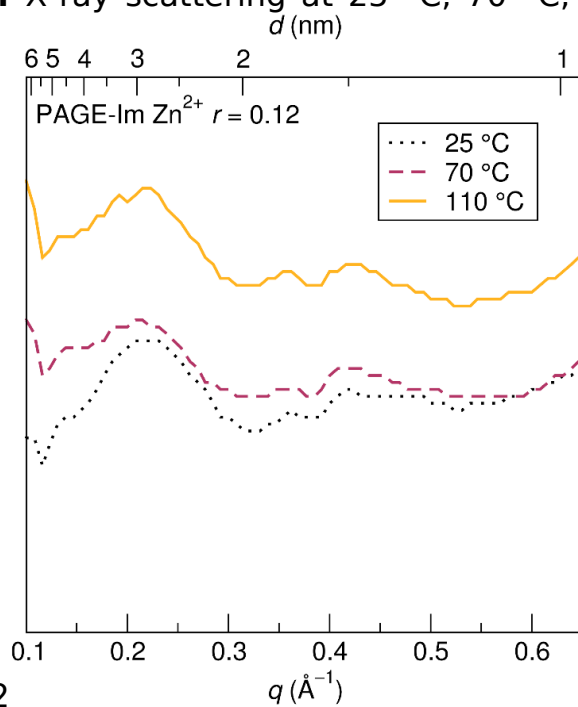**Figure S32.** X-ray scattering at 25 °C, 70 °C, and 110 °C for for PAGE-Im

Cu^{2+} r = 0.12

Figure S33. X-ray scattering at 25 °C, 70 °C, and 110 °C for for PAGE-Im Zn^{2+} r = 0.12.
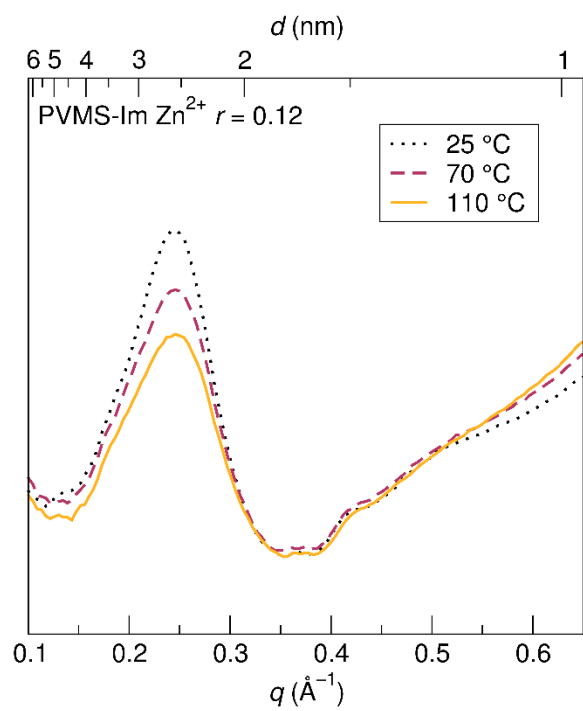
Figure S34. X-ray scattering at 25 °C, 70 °C, and 110 °C for for PVMS-Im Zn^{2+} r = 0.12.
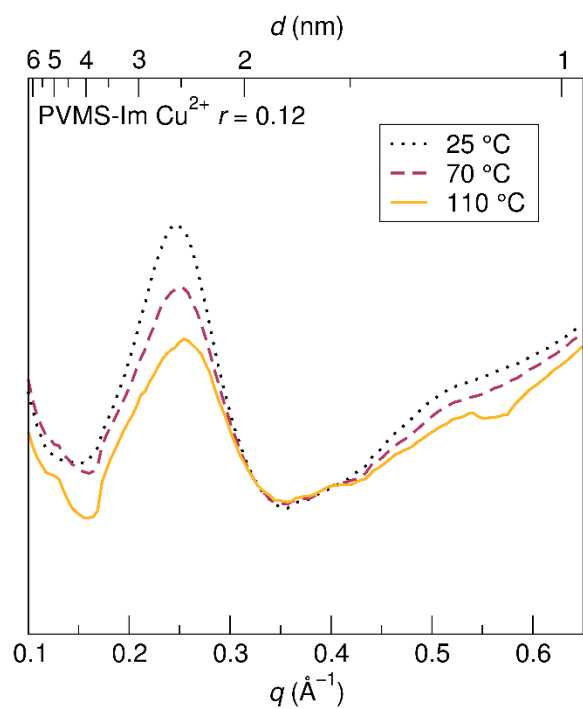
Figure S35. X-ray scattering at 25 °C, 70 °C, and 110 °C for for PVMS-Im Cu^{2+} r = 0.12.

Electron Paramagnetic Resonance

Field-Swept Echo (FSE)

The FSE spectra for PBD-Im and PAGE-Im were simulated with two components: i) resolved, isolated, Cu^{2+} ions with an axially elongated tetragonal ligand field ($g_\parallel > g_\perp$) and ii) a very broad, unresolved component.
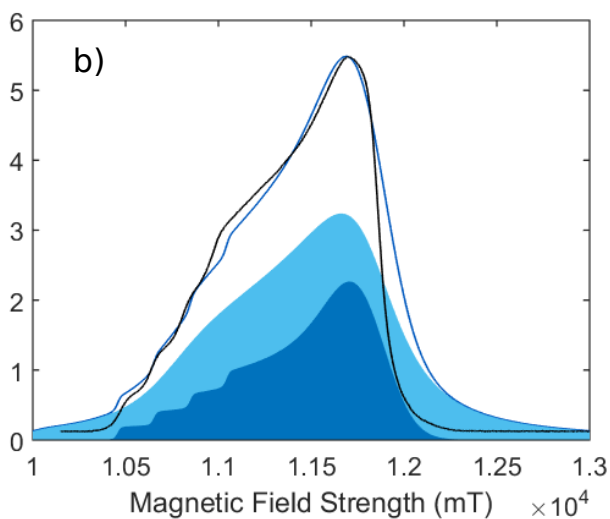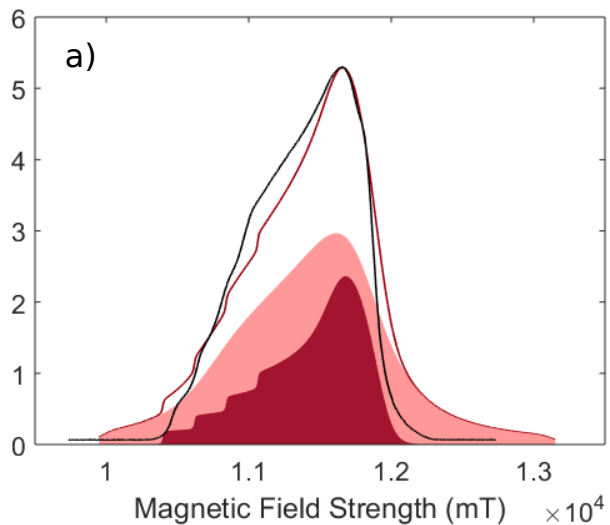
Figure S36. FSE spectra of a) PBD-Im Cu^{2+} and b) PAGE-Im Cu^{2+} and the individual spectral contributions from the narrow (isolated) and broad (aggregated) components.

Cu²⁺ calculations for dipolar broadening

A minimum concentration of Cu^{2+} ions that would cause dipolar broadening even in the absence of aggregation can be calculated assuming random close packing of Cu^{2+} spheres where the diameter of the Cu^{2+} sphere is the maximum separation distance that would cause dipolar broadening. Estimating this distance as $d = ¿15$ Å provides an easy baseline. Then, the volume of a Cu^{2+} sphere is

$$V_{Cu} = \frac{4}{3}\pi\left(\frac{d}{2}\right)^2 = 235.6\,\text{Å}^3$$

The packing density for a randomly close packed system of spheres is around 62.5%; thus, the total volume associated with a single Cu^{2+} ion (occupied volume and free volume) is

$$V_{total} = V_{Cu} \times \frac{100}{62.5} = 377\,\text{Å}^3$$

Thus, there must be at least one Cu^{2+} in a volume of 377 Å³ to observe dipolar broadening without ion aggregation. For a molar ratio of Cu^{2+} to imidazole of $r = 0.03$, and assuming a polymer density of around $1 g \times cm^{-3}$, and a monomer molar mass of 341.5 g/mol (PAGE-Im), we calculate a concentration of Cu^{2+} in the polymer as follows:

$$\frac{1\,g}{cm^3} \times \frac{cm^3}{10^{24}\,\text{Å}^3} \times \frac{1\,mol\,polymer}{341.5\,g} \times \frac{1\,mol\,imidazole}{1\,mol\,polymer} \times 0.03\,mol\,\frac{Cu^{2+}¿}{1\,mol\,imidazole} \times \frac{6.02 \times 10^{23}\,ions}{1\,mol\,Cu^{2+}¿}$$

$$¿0.00005\frac{Cu^{2+}¿}{\text{Å}^3} = 0.02\frac{Cu^{2+}¿}{377\,\text{Å}^3}¿¿$$

Thus, there is a much lower Cu^{2+} concentration in the polymer than what would be required to reach dipolar broadening without ion aggregation.

Hyperfine Sublevel Correlation Spectroscopy (HYSCORE)

Two-dimensional hyperfine sublevel correlation (HYSCORE) spectroscopy is a well-established technique that provides correlations between nuclear frequencies of different spin manifolds that interact with the unpaired electron.[1] In other words, it shows the NMR transitions of magnetically active nuclei interacting with the electron spin. The ¹⁴N nucleus is magnetically active, having a nuclear spin I = 1, in principle should result in six nuclear transitions if it interacts with an unpaired electron, three from each electron spin manifold, $m_s = \pm \frac{1}{2}$. For a disordered system such as PAGE-Im and PBD-Im, we expect complicated spectra, with large anisotropy leading to broadened peaks on the HYSCORE spectrum. These peaks contain information about the strength and nature of the hyperfine interaction between the unpaired spin in the Cu^{2+} nucleus and ¹⁴N. The hyperfine

interaction consists of two components, a_{iso} and T. a_{iso}, isotropic hyperfine coupling, is the Fermi contact term, which measures the spin density on the nucleus; while T, the dipolar coupling term, is inversely proportional to the distance between the electron and the nuclear spins ($T \propto 1/r^3$). In addition, since ^{14}N is a spin>1/2 (I=1) nucleus, it has a quadrupole moment that interacts with the electric field gradient (EFG) around the nucleus. The EFG tensor consists of 3 components. This EFG tensor can be fully described using two parameters, the nuclear quadrupole coupling constant, $K = e^2q_{zz}Q/h$, where e is the charge of the electron and Q is the nuclear electric quadrupole moment of the ^{14}N nucleus, and the asymmetry parameter, η. K measures the strength of interaction between the nuclear quadrupole moment and the EFG at the nucleus due to anisotropic distribution of charges. On the other hand, η measures the deviation of the distribution of charges from axial symmetry. K and η, along with a_{iso}, are used as signatures to identify the chemical environment around the ^{14}N nucleus, allowing its characterization. Extensive studies on Cu^{2+} and its interactions with the remote ^{14}N of the imidazole have allowed the elucidation of characteristic parameters for these systems.[2-6] Experiments at X-band (9.5 GHz) i.e. lower fields, typically fulfill the cancellation condition, where the three nuclear frequencies of each electron spin manifold, equal the three pure nuclear quadrupole resonance frequencies. In addition, a broadened double quantum transition, ν_{dq} is also observed. This frequency is correlated with K, a_{iso} and η using the following equation:

$$\nu_{dq\pm} = 2\sqrt{\left(\nu_I \pm \frac{a_{iso}}{2}\right)^2 + \left(\frac{K}{4}\right)^2 (3+\eta^2)}$$

Therefore, HYSCORE experiments that meet the cancellation conditions exhibit cross-peaks that correlate the three nuclear quadrupole resonances with ν_{dq}. Under X-Band conditions, this results in intrinsically complex spectra. When the cancellation condition not fulfilled, for example, at Q-Band frequencies (35 GHz), the HYSCORE spectra are greatly simplified and only exhibit a single pair of cross-peaks of the ν_{dq} transitions.[7] To simplify spectral analysis for such disordered systems, HYSCORE experiments were done at Q-Band frequencies.

As discussed previously, pulsed EPR allows the investigation of couplings at specific magnetic fields which correspond to different orientations of the electron spins in the polymers. The maximum peak occurs at a magnetic field (observer position) B_0 of 11650 G, which corresponds to a maximum population of spins at that particular orientation ($g_\perp$). Experimental spectra were also recorded at other observer field positions and decent fits were obtained for each of the polymers (Figure S37-38). The presence of characteristic dq cross-peaks at approximately [5.05 , 9.10] MHz and [9.10, 5.05] MHz in the strong coupling regime (A> $\nu_{14N}/2$) shows direct coordination of ^{14}N species to the unpaired electrons in Cu^{2+} in both polymer backbones. In addition, a broad anisotropic peak appears in the lower frequency regime centered around [3.6, 3.6] MHz for PAGE-Im Cu^{2+}. Cu^{2+}-imidazole systems typically show a_{iso} constants of 1.5-2 MHz, K values

between 1.4-2 MHz, and η parameters of 0.8-1, which were used as starting points for the simulated spectra.[2-6]

The experimental parameters, such as magnetic field, excitation frequency, number of points, dwell time, pulse width, and pulse delay, were taken directly from the HYSCORE experiments. Simulations of the spectra were iteratively done until a set of parameters was obtained that could reproduce the general features of the experimental spectra. The fit was performed using one type of ^{14}N species, where each of the five parameters (a_{iso}, T, K, η and β) were varied until a reasonable fit was observed for PBD-Im Cu^{2+} and fell within expected values for imidazole ligands (Table S2). The estimated a_{iso} value of 2 MHz corresponds to an unpaired spin density in the ^{14}N 2s orbital of ~ 1x 10^{-3} arising from the coordination of the imidazole ligand. The dipolar coupling term is not dominant for imidazole ^{14}N (0.15 MHz), while the K and η terms equal 1.8 MHz and 0.8 respectively. On the other hand, spectra for PAGE-Im Cu^{2+} could not be reproduced with the same parameters, especially at the low frequency region. Another ^{14}N component was therefore introduced to obtain a reasonable fit between the experimental and simulated spectra. The estimated parameters for this ^{14}N component also fall within the range of values that correspond to imidazole ligands, albeit with smaller a_{iso} (1.5 MHz) and K (1.5 MHz) values. The a_{iso} value describes the delocalization of electrons in the imidazole ring, therefore hinting towards slightly less delocalization for one of the imidazole environments. In addition, the K value is also smaller, suggesting a more symmetric environment. Finally, the orientation of this second imidazole, obtained from the Euler angle of the nuclear quadrupole tensor is almost perpendicular to that of the first. The principal axes system (PAS) specific to a molecule is used as the molecular frame reference. The PAS for Cu-imidazole complexes is typically the g parallel axis/symmetry axis. An estimation of the orientation of the hyperfine and the quadrupole coupling tensor (from the ^{14}N of the imidazole) can be found from the Euler angle (α, β, γ) because that angle can be thought of as a rotation angle to the molecular frame reference. In these simulations, the hyperfine angles did not significantly change the spectrum. However, varying the β angle of the quadrupole tensor played a role in the appearance of the peaks.
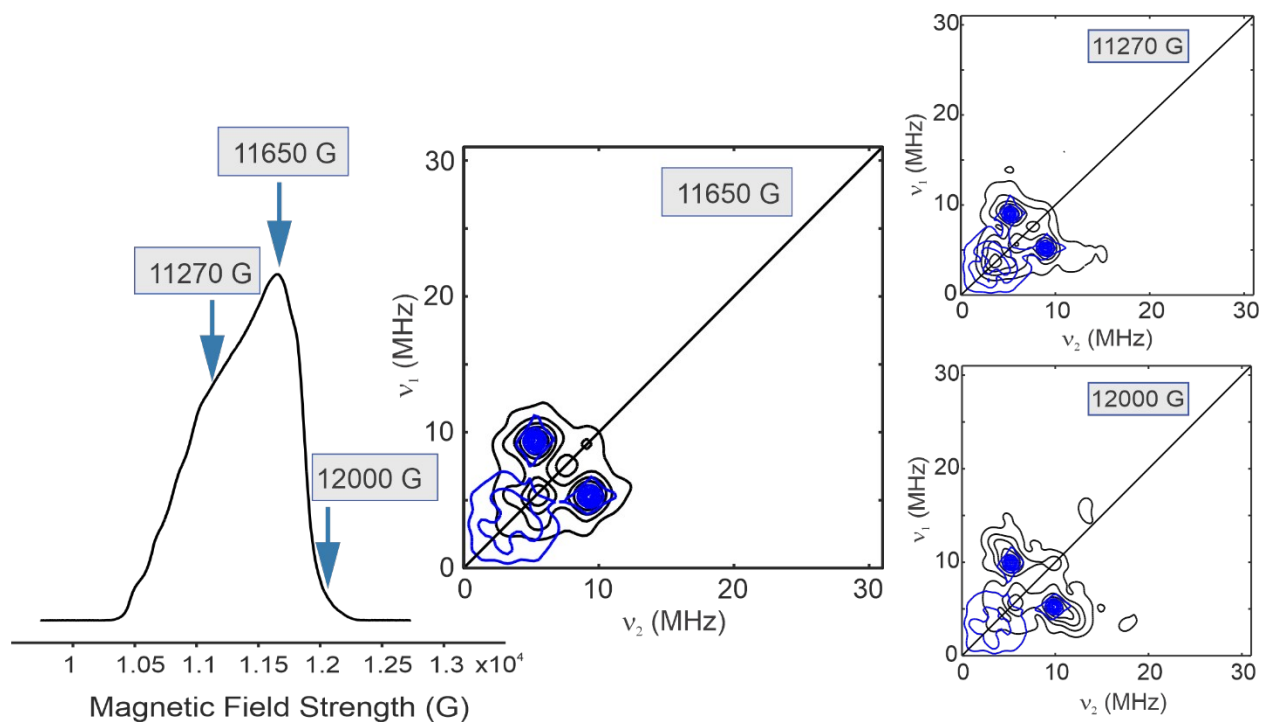
Figure S37. HYSCORE spectra of PBD-Im Cu^{2+} collected at different observer field positions and their corresponding simulations using the same set of parameters.
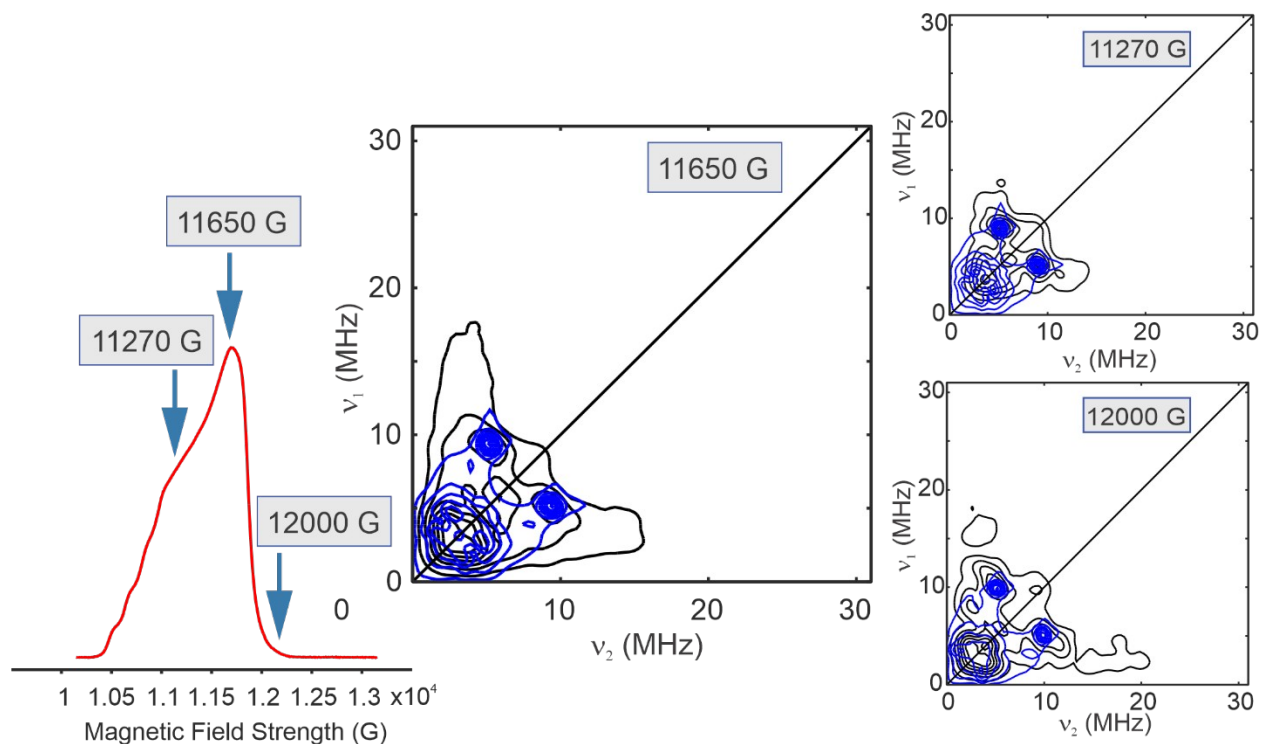
Figure S38. HYSCORE spectra of PAGE-Im Cu^{2+} collected at different observer field positions and their corresponding simulations using the same set of parameters.

Table S2. Estimated ^{14}N HYSCORE parameters from simulations of experimental data.

	a_{iso} (MHz)	T (MHz)	K	η	B(°)
PBD-Im Cu^{2+}	2	0.15	1.8	0.8	80
PAGE-Im Cu^{2+} (I)	1.5	0.2	1.5	0.8	0
PAGE-Im Cu^{2+} (II)	2	0.15	1.8	0.8	80

Field-theoretic (complex Langevin) simulations

Using Hubbard-Stratonovich transformations, the field-theoretic canonical partition function for the system of metal salt-coordinating polymers takes the form[8]

$$Z = Z_0 \int Dw_1 \int Dw_2 \int Dw_3 \int Dw_4 \int D\varphi \, e^{-H[w_1, w_2, w_3, w_4, \varphi]},$$

where φ is an electrostatic field that mediates the ion-ion, ion-dipole and dipole-dipole interactions, and w_1, w_2, w_3, and w_4 are exchange-mapped chemical potential fields that mediate contact interactions in the model. These contact interactions include the excluded volume interactions, as well as the Flory interactions between species A and B ($\chi_{AB} = 0.2$), between B and the cation ($\chi_{B+i=-20i}$), and between the cation and anion ($\chi_{\pm i=0.2i}$). The parameter $\chi_{\pm ii}$ does not have a significant effect on the structure but helps to reduce numerical scatter in the ion-ion structure factors that we measure. The term Z_0 contains ideal gas terms, normalization factors from the Hubbard-Stratonovich transforms, and self-interaction corrections, and its precise form is of no consequence here. The Hamiltonian $H[w_1, w_2, w_3, w_4, \varphi]$ is given by

$$H[w_1, w_2, w_3, w_4, \varphi] = \frac{\rho_0}{2} \sum_{i=1}^{4} \frac{1}{\sigma_i} \int dr\, w_i^2(r) + \frac{1}{8\pi l_B^{(0)}} \int dr\, |\nabla\varphi|^2 - n_p \ln Q_p[\Omega_A, \Omega_B] - n_{+i \ln Q_{+i i i i i}}$$

where Q_l is the single-molecule partition function for molecular species l and Ω_m is the local chemical potential field experienced by beads of species m. In general, the Ω_m contain contributions from all five auxiliary fields, and are given by

$$\Omega_A(r) = \sum_{i=1}^{4} \xi_i \Phi_{iA} \dot{w}_i(r) + \frac{\alpha_A}{2\beta e^2} |\nabla\dot{\varphi}|^2,$$

$$\Omega_B(r) = \sum_{i=1}^{4} \xi_i \Phi_{iB} \dot{w}_i(r) + \frac{\alpha_B}{2\beta e^2} |\nabla\dot{\varphi}|^2,$$

$$\Omega_\pm(r) = \sum_{i=1}^{4} \xi_i \Phi_{i\pm} \dot{w}_i(r) \mp iz\dot{\varphi}(r).$$

Here σ_i and Φ_{ij} are the eigenvalues and eigenvectors of the contact interaction matrix, respectively, and the parameter ξ_i takes the value 1 if $\sigma_i < 0$ and the value i if $\sigma_i > 0$. The overbar on the fields indicates a spatial convolution with the Gaussian smearing function, for example:

$$\dot{\varphi}(r) = \int dr' \Gamma(r - r') \varphi(r'),$$

where $\Gamma(r) = (2\pi a^2)^{-3/2} e^{-r^2/2a^2}$. Since the metal salt-coordinating polymer is architecturally a bottlebrush polymer, the single-chain partition function takes a form similar to that described in several recent works;[9-10] that is,

$$Q_p[\Omega_A, \Omega_B] = \frac{1}{V} \int dr\, q_{bb}(r, N_{bb}),$$

where $q_{bb}(r, s)$ is the forward backbone propagator. In general, in order to sample the trajectories of the fields via the complex Langevin scheme, and also to calculate the polymer densities, we must compute the forward and backward backbone propagators $q_{bb}(r, s)$ and $\tilde{q}_{bb}(r, s)$, respectively, as well as the forward and backward side-chain propagators $q_{sc}(r, s)$ and $\tilde{q}_{sc}(r, s)$, respectively. If there are $N_{bb}/\tau - 1$ equally-spaced side-chains (i.e. a junction every $\Delta s = \tau$ along the backbone), the following modified diffusion equation must be solved in sections of length τ for the forward backbone propagator $q_{bb}(r, s) = q_{bb}^{(j)}(r, s)$, where $j\tau \leq s < (j+1)\tau$:

$$\frac{\partial}{\partial s} q_{bb}^{(j)}(r, s) = \left[\frac{b^2}{6}\nabla^2 - \Omega_A(r)\right] q_{bb}^{(j)}(r, s),$$

with a j-dependent initial condition given by

$$q_{bb}^{(j)}(r,j\tau)=\begin{cases}1,\wedge j=0\\q_{bb}^{(j-1)}(r,j\tau)q_{sc}(r,N_{sc}),\wedge j\neq 0\end{cases}$$

and a similar equation for the backward backbone propagator:

$$\frac{\partial}{\partial s}\tilde{q}_{bb}^{(j)}(r,N_{bb}-s)=\left[\frac{b^2}{6}\nabla^2-\Omega_A(r)\right]\tilde{q}_{bb}^{(j)}(r,N_{bb}-s),$$

with the initial condition

$$\tilde{q}_{bb}^{(j)}(r,N_{bb}-j\tau)=\begin{cases}1,\wedge j=0\\\tilde{q}_{bb}^{(j-1)}(r,N_{bb}-j\tau)q_{sc}(r,N_{sc}),\wedge j\neq 0\end{cases}$$

and we also note that if the polymer is symmetric along the backbone contour, as it is in our case, then $q_{bb}(r,s)=\tilde{q}_{bb}(r,N_{bb}-s)$ by symmetry and the backward backbone propagator need not be computed. The forward side-chain propagator, which we define to propagate starting from the side-chain end, satisfies

$$\frac{\partial}{\partial s}q_{sc}(r,s)=\left[\frac{b^2}{6}\nabla^2-\Omega_m(r)\right]q_{sc}(r,s),$$

where

$$\Omega_m(r)=\begin{cases}\Omega_B(r),\wedge s<N_{sc}/2\\\Omega_A(r),\wedge s\geq N_{sc}/2\end{cases}$$

and with the initial condition $q_{sc}(r,0)=1$. The backward propagators for the side-chains $\tilde{q}_{sc}^{(j)}(r,s)$, where $j=1,2,\dots,N_{bb}/\tau-1$, acquire a dependence on the position of their junction along the backbone through their initial condition, and satisfy

$$\frac{\partial}{\partial s}\tilde{q}_{sc}^{(j)}(r,N_{sc}-s)=\left[\frac{b^2}{6}\nabla^2-\Omega_m(r)\right]\tilde{q}_{sc}^{(j)}(r,N_{sc}-s),$$

where

$$\Omega_m(r)=\begin{cases}\Omega_A(r),\wedge s<N_{sc}/2\\\Omega_B(r),\wedge s\geq N_{sc}/2\end{cases}$$

and with the initial condition $\tilde{q}_{sc}^{(j)}(r,N_{sc})=q_{bb}(r,j\tau)\tilde{q}_{bb}(r,N_{bb}-j\tau)$. The single-molecule partition functions for the cation and anion take a simpler form, given by

$$Q_\pm[\Omega_\pm]=\frac{1}{V}\int dr\, e^{-\Omega_\pm(r)}.$$

45

In order to sample this unapproximated field theory we employ complex Langevin sampling, in which the auxiliary fields are promoted to be complex variables that evolve according to the following equations of motion:

$$\frac{\partial w_i(r,t)}{\partial t}=-\Lambda_{w_i}\frac{\delta H\big[[w],\varphi\big]}{\delta w_i(r,t)}+\eta_{w_i}(r,t),$$

$$\frac{\partial \varphi(r,t)}{\partial t}=-\Lambda_{\varphi}\frac{\delta H\big[[w],\varphi\big]}{\delta \varphi(r,t)}+\eta_{\varphi}(r,t),$$

where the $\eta_j(r,t)$ are real-valued Gaussian-distributed white noise variables (j runs over the set of auxiliary fields) with zero mean $\langle\eta_j(r,t)\rangle=0$ and satisfying the fluctuation-dissipation theorem $\langle\eta_i(r,t)\eta_j(r',t')\rangle=2\Lambda_j\delta_{ij}\delta(r-r')\delta(t-t')$. As the complex Langevin trajectories are sampled, we compute operator averages by leveraging the ergodic principle.

Species polarizabilities in field-theoretic simulations

In our field-theoretic model, bead species *A* is either *PBD-like* or *PAGE-like* and species *B* is *imidazole-like* (*Im-like*). The PBD and PAGE backbones in the experimental section of this work have measured dielectric constants of $\epsilon_{PBD}=2.3$ and $\epsilon_{PAGE}=6.0$, as reported in Table 1. The dielectric constant of liquid 1-methylimidazole (MeIm) has been reported to be as large as $\epsilon_{MeIm}\approx40$.[11] We note that fluid dielectric constants are typically sensitive to temperature, pressure, and other variables such as chain connectivity and addition of salt, so we do not attempt to achieve quantitative agreement with literature or reported values. Rather, we grant these beads molecular polarizabilities such that they have qualitatively correct emergent dielectric properties: most importantly, that $\epsilon_{PBD-like}<\epsilon_{PAGE-like}<\epsilon_{\Im-like}$ for pure fluid phases of the respective bead types, and that the dielectric constants have a reasonable magnitude when compared to the above reported and measured values. To estimate the emergent dielectric properties of the beads in our model, we can use the mean-field expression for the dielectric constant in the polarizable field theory

$$\epsilon_{MF}=1+4\pi\rho_0\alpha_v,$$

where α_v is the polarizability volume. We note that the true dielectric constant in field-theoretic simulations (FTS) will differ somewhat from the above mean-field expression, due to correlation effects that mean-field theory does not capture. In this work we use $\alpha_v^{(PBD-like)}=0.011\,b^3$, $\alpha_v^{(PAGE-like)}=0.108\,b^3$, and $\alpha_v^{(\Im-like)}=0.541\,b^3$. Figure S22, below, shows the dielectric functions directly measured from FTS, for the PBD-like, PAGE-like and Im-like bead types, along with the corresponding mean-field dielectric functions. The pure-fluid dielectric constants, which correspond to the

dielectric function at $k=0$, are roughly $\epsilon_{PBD-like} \approx 2$, $\epsilon_{PAGE-like} \approx 10$, and $\epsilon_{\Im-like} \approx 47$.
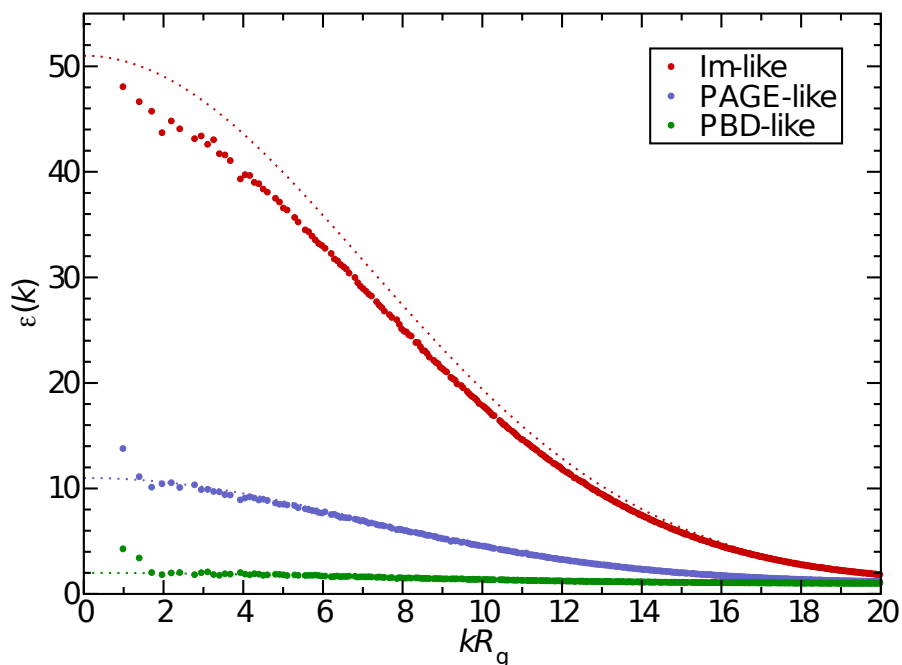

Figure S39. Dielectric function of a pure fluid phase of Im-like, PAGE-like and PBD-like monomers, at a density of $\rho_0 = 7.35 b^{-3}$, as measured in field-theoretic simulations. Dotted lines are the mean-field estimates.

Numerical details of field-theoretic simulations

The simulations presented in this work were conducted in a cubic box with dimensions $(6.4 R_g)^3$ and periodic boundary conditions. The spatial collocation mesh resolution was chosen to be $\Delta x = a = 0.1 R_g$, which is sufficient to resolve the smallest-scale features in our coarse-grained model. We solve the modified diffusion equations for the chain propagators using a pseudospectral operator-splitting approach with a chain contour resolution of $\Delta s = 0.005 N_{bb}$. The CL equations of motion were propagated using the exponential time difference (ETD) algorithm with a time step $\Delta t = 0.05$, and using mobility coefficients of unity for all w fields and a mobility coefficient $\Lambda_\varphi = 20$ which helps to accelerate thermalization of the electrostatic field. In all cases, the system is initialized in a random disordered configuration in which the fields have been equilibrated (this involves a warmup simulation on the order of 10^6 timesteps). All simulations were performed on NVIDIA Tesla M2070, M2075, C2070, K80, P100 or V100 graphics processing units (GPUs).

We use a low-variance structure factor operator, which is defined in Reference 11,[12] to compute the cation-cation structure factors $S_{++}(k)$. The

structure factor at each state point in Figure 7 is the result of an average over between 3 and 5 independent field-theoretic simulations, each of which is initialized in an equilibrated, random disordered configuration, and thermally averaged for on the order of 10^6 time-steps. The cation density calculations are the result of thermal averages of the cation density operator $\widetilde{\rho}_{+¿(r)¿}$, which is given by

$$\widetilde{\rho}_{+¿}(r)=\frac{n_{+¿}}{V\,Q_{+¿}e^{-\Omega_{+¿(r)¿}}}¿¿,$$

and we perform the thermal average of this operator over 2×10^5 time-steps for both the PBD-Im-like and PAGE-Im-like polymer to generate the cation density images in Figure 8.

Anion-anion structure factor

Figure S40 shows the comparison between the anion-anion structure factor and cation-cation structure factor for the PBD-like polymer.
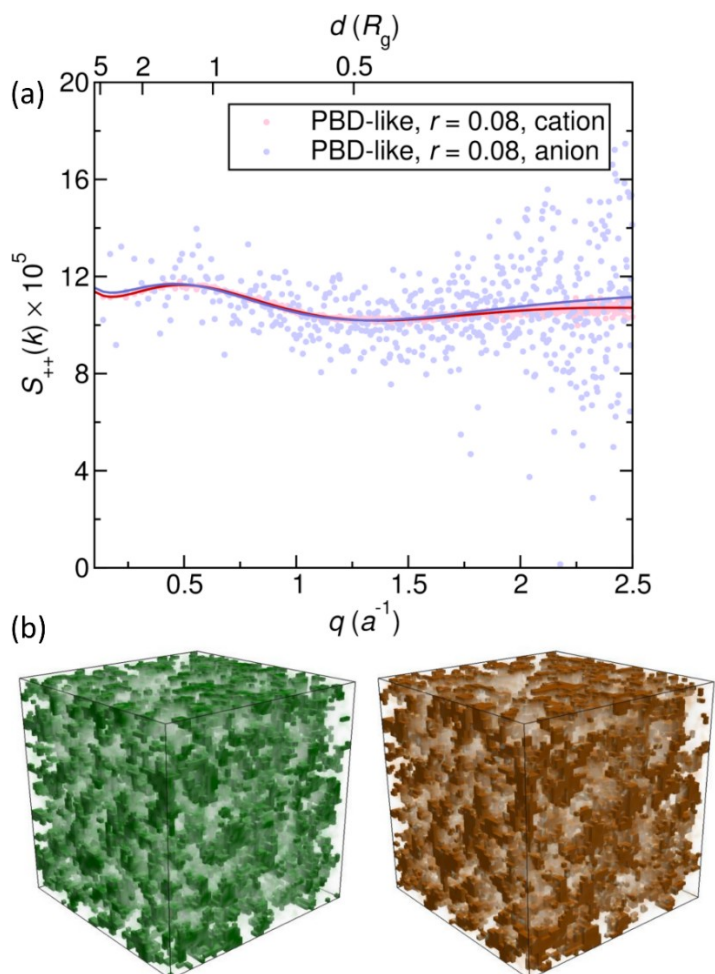

Figure S40. (a) Cation-cation and anion-anion structure factors show similar behavior with a peak indicating ion aggregation. (b) Ion channels, identified by the criterion $\phi_{+¿-¿(r)\geq¿¿}$, form a percolating network for both cations and anions.

References

1. Shane, J. J.; Höfer, P.; Reijerse, E. J.; de Boer, E., Hyperfine Sublevel Correlation Spectroscopy (HYSCORE) of Disordered Solids. *J. Magn. Reson.* **1992,** *99*, 596-604.
2. McCracken, J.; Pember, S.; Benkovic, S. J.; Villafranca, J. J.; Miller, R. J.; Peisach, J., Electron Spin-Echo Studies of the Copper Binding Site in Phenylalanine Hydroxylase from Chromobacterium Violaceum. *J. Am. Chem. Soc.* **1988,** *110*, 1069-1074.
3. Jiang, F.; McCracken, J.; Peisach, J., Nuclear Quadrupole Interactions in Copper(II)-Diethylenetriamine-Substituted Imidazole Complexes and in Copper(II) Proteins. *J. Am. Chem. Soc.* **1990,** *112*, 9035-9044.
4. Jiang, F.; Karlin, K. D.; Peisach, J., An Electron Spin Echo Envelope Modulation (ESEEM) Study of Electron-Nuclear Hyperfine and Nuclear Quadrupole Interactions of dz2 Ground State Copper(II) Complexes with Substituted Imidazoles. *Inorg. Chem.* **1993,** *32*, 2576-2582.
5. Kofman, V.; Farver, O.; Pecht, I.; Goldfarb, D., Two-Dimensional Pulsed EPR Spectroscopy of the Copper Protein Azurin. *J. Am. Chem. Soc.* **1996,** *118*, 1201-1206.
6. Grommen, R.; Manikandan, P.; Gao, Y.; Shane, T.; Shane, J. J.; Schoonheydt, R. A.; Weckhuysen, B. M.; Goldfarb, D., Geometry and Framework Interactions of Zeolite-Encapsulated Copper(II)−Histidine Complexes. *J. Am. Chem. Soc.* **2000,** *122*, 11488-11496.
7. Taguchi, A. T.; O'Malley, P. J.; Wraight, C. A.; Dikanov, S. A., Hyperfine and Nuclear Quadrupole Tensors of Nitrogen Donors in the QA Site of Bacterial Reaction Centers: Correlation of the Histidine Nδ Tensors with Hydrogen Bond Strength. *J. Phys. Chem. B* **2014,** *118*, 9225-9237.
8. Fredrickson, G. H., *The Equilibrium Theory of Inhomogeneous Polymers*. Oxford University Press: 2006.
9. Levi, A. E.; Lequieu, J.; Horne, J. D.; Bates, M. W.; Ren, J. M.; Delaney, K. T.; Fredrickson, G. H.; Bates, C. M., Miktoarm Stars via Grafting-Through Copolymerization: Self-Assembly and the Star-to-Bottlebrush Transition. *Macromolecules* **2019,** *52*, 1794-1802.
10. Panagiotou, E.; Delaney, K. T.; Fredrickson, G. H., Theoretical Prediction of an Isotropic to Nematic Phase Transition in Bottlebrush Homopolymer Melts. *J. Chem. Phys.* **2019,** *151*, 094901.
11. Zhang, H.; Geise, G. M., Modeling the Water Permeability and Water/Salt Selectivity Tradeoff in Polymer Membranes. *J. Membrane Sci.* **2016,** *520*, 790-800.
12. Düchs, D.; Delaney, K. T.; Fredrickson, G. H., A Multi-Species Exchange Model for Fully Fluctuating Polymer Field Theory Simulations. *J. Chem. Phys.* **2014,** *141*, 174103.